Dislocation detection of gas turbine materials using a nonlinear ultrasound modulation technique

Frank Mevissen[1] and Michele Meo[2]
[1]Materials Research Centre, Department of Mechanical Engineering,
University of Bath, Bath, BA2 7AY, UK
[2] Department Aeronautics and Astronautics, University of Southampton, UK
E-mail: f.mevissen@bath.ac.uk, [2] Correspondence: m.meo@soton.ac.uk

Abstract

Industrial gas turbines are used for generating electricity or driving other turbomachinery with the continuous development goal of further increasing machine efficiency. This is primarily achieved by raising the pressure ratio generated in the compressor and by increasing the turbine inlet temperature. Consequently, the hot gas components in gas turbines are subjected to extreme loads and the need for non-destructive testing and structural health monitoring techniques is becoming increasingly important for the maintain these components. An important indicator for assessing the structural integrity is the determination of the initial plastic deformation.

In this paper, a new method for the detection of plasticity was developed, which is based on a nonlinear ultrasonic two-frequency excitation. The one-dimensional wave equation was solved with a two-frequency excitation and combined with the expanded dislocation theory. As a result, various nonlinearity parameters were defined, showing a clear increasing or a decreasing behaviour with increasing plastic strain. This was experimentally proven with flat tensile specimen made of stainless steel and Inconel 718 (metal plates and additively manufactured). The new indicators allows the possibility to efficiently detect the initial plastic deformation in gas turbine components.

1. Introduction

Depending on the operating mode of a gas turbine, different failure modes exists, which could lead to component malfunctions or failures. These failures are mainly rupture, creep deflection, high-cycle fatigue, oxidation, erosion, corrosion, rubbing/wear, foreign object damage, thermal mechanical failure and combined failure mechanism [1]. Therefore, the detection of initial plastic deformation is of enormous importance, as this would be a direct indication of one of the failure modes described. Modern ultrasound techniques are very promising for the detection of failures. In 1966, Langenecker proved that the physical changes in deformed materials can be detected using ultrasonic waves [2]. According to the work of Yang et al., plastic deformation and fatigue damage, in addition to the intrinsic nonlinearity due to the interatomic and molecular forces, can be a cause of the nonlinearities in materials. It was shown that fatigue life and plastic deformation can be assessed based on the change in the nonlinear properties of ultrasonic waves [3], and this topic was further summarized in a review paper [4]. The influence on the superposition of ultrasonic signals with the unidirectional applied load in the plastic deformation area was investigated [5]. Estrin developed a unified elastic-viscoplastic constitutive model, presenting a combination of kinetic equation that describes the mechanical response of a material at a given microstructure in terms of dislocation slip [6]. Jhang et al. developed a new approach to effectively assess material degradation. The nonlinear effect of ultrasonic waves was proposed for failure interpretation, where harmonic waves of higher order were generated [7, 8]. The influence of superimposed ultrasonic vibrations on plastically compressed aluminium samples was examined [9, 10]. Ramkumar et al. studied the second harmonic frequency to detect dislocations in materials [11]. Pruell et al. detected experimentally generated material nonlinearities in metal plates with Lamb waves. It was demonstrated that the acoustic nonlinearity parameters increase linearly with the distance of propagation [12]. Deng et al. examined the nonlinear effect of the propagation of the primary Lamb wave in assessing fatigue damages. This was analytically analysed for solid plates [13]. The acoustic nonlinearity generated by Lamb waves was also used to determine the degree of plasticity of metal samples [14] and to detect thermal aging [15]. Rao et al. examined various plasticized aluminium samples with longitudinal waves and surface acoustic waves (SAW). With the second harmonic nonlinearity parameter, the dislocations in materials can be described [16]. A method was developed to detect micro-damages caused by high-cycle fatigue. Therefore, longitudinal waves were sent diagonally into the component and the formed acoustic nonlinearities were used for evaluation [17-19]. To detect material plasticization through low-cycle fatigue, nonlinear Rayleigh waves were used [20, 21]. Dutta et al. examined the acoustoplastic effect in metals. When ultrasonic waves are used it may lead to additional stresses in the component or to heating, which was tested in-situ with tensile tests [22]. Fatigue damages were theoretically predicted by nonlinear ultrasonic techniques and verified with simulations and experiments [23]. Xiang et al. used nonlinear ultrasound techniques to detect creep degradation in titanium alloys. A change in the acoustic nonlinearity with increasing creep load time was demonstrated experimentally. It was revealed that the dislocation mechanism is the decisive factor in the change in nonlinearity during material creep [24]. This dislocation theory was used for the physical description of plastic deformations in materials.

Hikata et al. used the second harmonic nonlinearity parameter to prove dislocation contributions in materials. A physical model with constant line tension was combined with the one-dimensional wave equation. The amplitudes of the fundamental frequency and the second harmonic frequency measured in experiments were used as dislocation indicators. Therefore, direct conclusions were drawn about dislocations in materials [25, 26]. Cantrell et al. established a model to consider the effects of the grid resistance on the deflection of the dislocations [27, 28]. Cash et al. developed a system to allow variable line energy compared to other works. This led to the implementation of the Poisson's ratio in the derivation [29, 30]. Xiang et al. proposed an analytical model based on the dislocation line energy and the variable line stress [31]. Zhang et al. examined dislocation lines with arbitrary orientation. The changed acoustic nonlinearities depend on the dislocation line and were proven experimentally on stainless steel samples [32, 33]. Zhu et al. studied the plastic deformation of martensitic stainless steel based on the concept of dislocation [35]. Gao et al. examined acoustic nonlinearity as a signature of microstructure defects on propagating ultrasound [35]. Xiang et al. [31] and Oruganti et al. [11] studied the influence of mixed dislocations on the local stresses that were prestressed in a certain direction.

As a result, an asymmetrical dislocation movement occurs. This asymmetry in the tension field leads to a back stress.

The nonlinearity parameters presented in the literature overview, were defined using the model of the one-dimensional wave equation (amplitude comparison) [26, 27] or directly using the nonlinear stress-strain behaviour (coefficient comparison) [27, 29, 31, 33, 35].

The aim of this study is a clear identification of plastic deformation at an early stage and an effective assessment of the degree of plasticization. Therefore, the analysis of two superimposed ultrasonic frequencies was further developed, which was successfully used to detect cracks [36, 37]. On this basis, the dislocation theory of Hikata et al. was extended and combined with the model of the one-dimensional wave equation up to the third-order of nonlinearity. The newly derived nonlinearity parameters were compared with experimental data. Flat tensile specimen made of stainless steel, Inconel 718 plate material and Inconel 718 selective laser melting (SLM) material were used for the experimental work. These samples were deformed with increasing plastic strain and then compared with reference samples.

2. Analytical approach

A physical description of the dislocation process is required to evaluate the plastic deformation meaningfully. In this section, the dislocation theory is expanded to a function of higher orders. This is combined with the one-dimensional wave equation with two superimposed excitation frequencies up to the third-order of nonlinearity to derive novel nonlinearity parameters for the evaluation of plasticity in materials. The derivations are made with ultrasound excitation in the direction of the tensile load vector and perpendicular to it.

2.1. Dislocation

Frank and Reed developed the dislocation multiplication in 1950 with the description of sliding in isotropic materials [38]. If a body is plastically deformed under a load, dislocations form in a slip plane (Figure 1). The dislocation density increases and finally changes the crystal structure. The applied tensile load σ_{xx} and the resolved shear stress τ_R have the following relationship [25]:

$$\sigma_{xx} = \frac{\tau_R}{R}, \tag{1}$$

where R is the Schmid factor, which describes the resolved shear stress τ_R in a sliding system of a crystalline material that is stressed by an external load. This factor also determines the position of the slip plane relative to the stressed body, which is why the position indices for τ_R and for the description of the dislocation are not used.

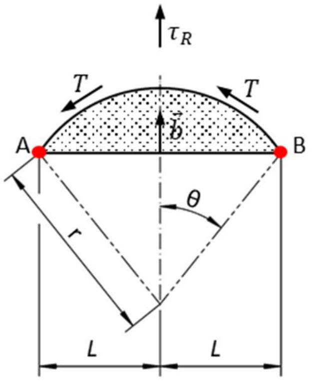

Figure 1. Dislocation scheme.

If the shear stress is increased, the dislocation begins in the slip plane and forms a curve, where the endpoints A and B remain fixed and L is the length of the bowing dislocation segment. If the shear force exceeds the restoring force, the dislocation line is deformed in all directions ($\tau_R > \frac{\mu b}{R}$). T is the line tension, which is assumed constant regardless of the orientation, μ is the shear modulus, b is the Burgers vector. The same line energy required by the edge dislocation leads to a circular arc with a constant radius of curvature.

The dislocation shear strain γ^d is defined as [25]:

$$\gamma^d = \frac{\Lambda b}{2L} A_d, \tag{2}$$

where Λ is the dislocation density and A_d the swept out area which is defined as:

$$A_d = r^2 \left(\theta - \frac{1}{2} sin(2\theta)\right), \tag{3}$$

where θ is the angle between the Burgers vector and the dislocation line. Assuming small dislocation densities and an independent line tension T of the radius r, the relationship for the shear stress is defined as [26]:

$$\tau_R = \frac{\mu b}{2r}. \tag{4}$$

For small dislocations $\theta \approx \frac{L}{r}$ is valid. With Equations (2), (3) and (4), the sine series expansion results:

$$\gamma^d = \frac{2}{3}\frac{\Lambda L^2}{\mu}\tau_R - \frac{8}{15}\frac{\Lambda L^4}{\mu^3 b^2}\tau_R^3 + \frac{64}{315}\frac{\Lambda L^6}{\mu^5 b^4}\tau_R^5. \tag{5}$$

If the tensile stress σ_{xx} acts on a body, it is deformed in the main direction vectors (Figure 2).

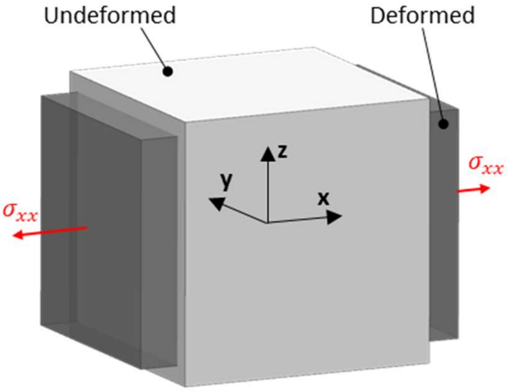

Figure 2. Body deformation.

If, in addition, the applied tensile stress $\sigma_{xx} > R_{p0.2}$ (yield strength), this leads to dislocations and elastic and inelastic strains in the main directions of the coordinate system. The total strain ε_{xx} is a summation of the elastic lattice strain, ε_x^l and plastic strain, ε_x^d. The plastic dislocation strain is defined as $\varepsilon_x^d = \Omega\gamma^d$, where Ω the conversion factor from shear strain to longitudinal strain [26], which results in:

$$\varepsilon_{xx} = \varepsilon_x^l + \Omega\gamma^d. \tag{6}$$

Therefore, the normal strains for this load case are defined as:

$$\varepsilon = \begin{bmatrix} \varepsilon_x^l + \Omega\gamma^d & 0 & 0 \\ 0 & -\nu(\varepsilon_x^l + \Omega\gamma^d) & 0 \\ 0 & 0 & -\nu(\varepsilon_x^l + \Omega\gamma^d) \end{bmatrix}, \tag{7}$$

where ν is the Poisson's ratio, which in real systems increases slightly in comparison before and after the applied load during plastic deformation [39, 40]. For this application, due to the negligible influence, it is assumed that the values before and after the elastic-plastic deformation remain the same.

Figure 3a illustrates the deformation of the lattice structure by the load σ_{xx}, whereby elastic strain (ε_x^l) and plastic strain (ε_x^d) appear together during loading. In the stress-strain diagram in Figure 3b, it becomes clear that the elastic strain component increases in the plastic deformation range due to the strain hardening and leads to a higher yield strength [41].

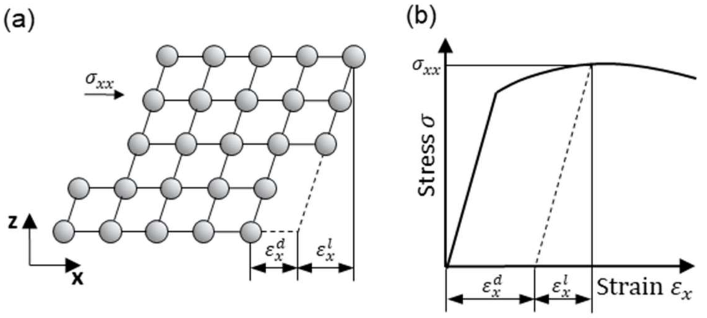

Figure 3. General strains: (a) lattice structure; (b) stress-strain diagram.

Using the first Piola-Kirchhoff stress formulation, the following expression for the stress σ_{xx} is given, which describes the elastic part in the plastic deformation area [27, 35]:

$$\sigma_{xx} = A_2^H \varepsilon_x^l + \frac{1}{2} A_3^H {\varepsilon_x^l}^2, \tag{8}$$

where A_2^H and A_3^H are the second- and third-order Huang coefficients that use the notation in accordance with [31, 34]. The second-order elastic coefficient A_2^H is also referred to as P-wave moduli, which describes the mechanical stress required to obtain a unit strain ε_{xx} if ε_{yy} and ε_{zz} are constrained to zero by the surrounding material [44] (Equation (9)):

$$A_2^H = \lambda + 2\mu, \tag{9}$$

where λ and μ are the Lamé constants, while the variable μ also represents the shear modulus. The third-order elastic coefficient is defined as follows [42] (Equation (10)):

$$A_3^H = 3A_2^H + 2(l + 2m), \tag{10}$$

where l and m are two of the three Murnaghan constants.

Different notations are used in literature for the second- and third-order coefficient (E_2 resp. E_3 [25, 33, 35], A_2^e resp. A_3^e [32], A_{11} resp. A_{111} [43] and A_{66} resp. A_{666} [29, 30]).

With Equations (1), (5), (7) and (8), the following relation arises for the normal strain tensor for higher orders with the dislocations variables:

$$\boldsymbol{\varepsilon} = \left(\left(-\frac{1}{A_2^H} - \frac{2}{3}\frac{\Omega \Lambda L^2 R}{\mu}\right)\sigma_{xx} - \frac{A_3^H}{2(A_2^H)^3}\sigma_{xx}^2 - \frac{8}{15}\frac{\Omega \Lambda L^4 R^3}{\mu^3 b^2}\sigma_{xx}^3 + \frac{64}{315}\frac{\Omega \Lambda L^6 R^5}{\mu^5 b^4}\sigma_{xx}^5\right)\begin{bmatrix} 1 & 0 & 0 \\ 0 & -\nu & 0 \\ 0 & 0 & -\nu \end{bmatrix}. \tag{11}$$

The further derivations are divided depending on the direction of the ultrasonic excitation (Figure 4):

- Tensile load (σ_{xx}) and ultrasonic pressure ($\Delta\sigma_{xx}^{u}$) collinear in x-direction (‖) (Figure 4a).
- Tensile load (σ_{xx}) in x-direction and ultrasonic pressure ($\Delta\sigma_{zz}^{u}$) orthogonal in z-direction (⊥) (Figure 4b).

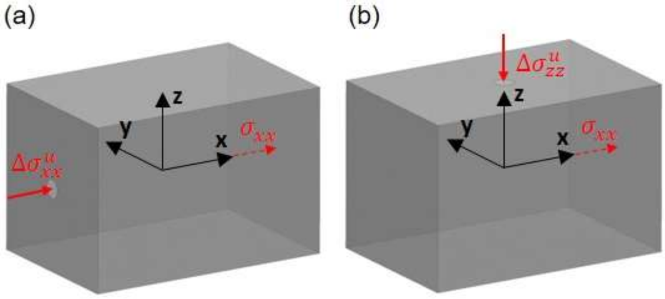

Figure 4. Ultrasonic excitation: (a) collinear excitation, ‖; (b) orthogonal excitation, ⊥.

If the vectors of the tensile stress and the ultrasonic pressure are superimposed (collinear excitation), a quasi-one-dimensional model can be assumed for the further steps [25,29-35, 43]. The body experiences an additional, superimposed strain ($\Delta\varepsilon_{xx}^{u}$) from the longitudinal, ultrasonic signal ($\Delta\sigma_{xx}^{u}$) [26]:

$$\Delta\sigma_{xx}^{u} = \frac{\partial\sigma_{xx}}{\partial\varepsilon_{xx}}\Delta\varepsilon_{xx}^{u} + \frac{1}{2}\frac{\partial^{2}\sigma_{xx}}{\partial{\varepsilon_{xx}}^{2}}(\Delta\varepsilon_{xx}^{u})^{2} + \frac{1}{6}\frac{\partial^{3}\sigma_{xx}}{\partial{\varepsilon_{xx}}^{3}}(\Delta\varepsilon_{xx}^{u})^{3}. \tag{12}$$

This expression described the behaviour of a small stress $\Delta\sigma_{xx}^{u}$ under the influence of a preload σ_{xx}. According to the rules for derivatives of inverse functions, this yields to:

$$\Delta\sigma_{xx}^{u} = \underbrace{\left(\frac{\partial\varepsilon_{xx}}{\partial\sigma_{xx}}\right)^{-1}}_{\alpha_{d}^{\parallel}}\Delta\varepsilon_{xx}^{u} + \frac{1}{2}\underbrace{\left(-\frac{\partial^{2}\varepsilon_{xx}}{\partial{\sigma_{xx}}^{2}}\left(\frac{\partial\varepsilon_{xx}}{\partial\sigma_{xx}}\right)^{-3}\right)}_{\beta_{d}^{\parallel}}(\Delta\varepsilon_{xx}^{u})^{2} + \frac{1}{6}\underbrace{\left(-\frac{\partial^{3}\varepsilon_{xx}}{\partial{\sigma_{xx}}^{3}}\left(\frac{\partial\varepsilon_{xx}}{\partial\sigma_{xx}}\right)^{-4} + 3\left(\frac{\partial^{2}\varepsilon_{xx}}{\partial{\sigma_{xx}}^{2}}\right)^{2}\left(\frac{\partial\varepsilon_{xx}}{\partial\sigma_{xx}}\right)^{-5}\right)}_{\gamma_{d}^{\parallel}}(\Delta\varepsilon_{xx}^{u})^{3}, \tag{13}$$

where $\alpha_{d}^{\parallel}$ is the first coefficient, $\beta_{d}^{\parallel}$ is the second-order nonlinearity coefficient and $\gamma_{d}^{\parallel}$ is the third-order nonlinearity coefficient. In the linear elastic deformation range, $\alpha_{d}^{\parallel}$ would be referred to as the Young's modulus, *E*, in which both (α_{d} and *E*) are shown as comparison in Appendix A. It is assumed that the nonlinear part ($\alpha_{d}^{\parallel}$, $\beta_{d}^{\parallel}$ and $\gamma_{d}^{\parallel}$) is caused by the dislocation in the material. Therefore, Equation (13) is solved by inserting the ε_{xx}-component of Equation (11) and the following relations result for the coefficients $\alpha_{d}^{\parallel}$, $\beta_{d}^{\parallel}$ and $\gamma_{d}^{\parallel}$:

$$\alpha_d^{\parallel} = P_1^{-1},$$
$$\beta_d^{\parallel} = \frac{P_2}{P_1^3},$$
$$\gamma_d^{\parallel} = \frac{P_3}{P_1^4} - \frac{3P_2^2}{P_1^5}.$$

The factors $\mathrm{P}_1, \mathrm{P}_2$ and P_3 are defined as:

(14)

$$P_1 = \frac{1}{A_2^H} + \frac{2}{3}\frac{\Omega\lambda L^2 R}{\mu} - \frac{A_3^H}{\left(A_2^H\right)^3}\sigma_{xx} - \frac{8}{5}\frac{\Omega\lambda L^4 R^3}{\mu^3 b^2}\sigma_{xx}^2 + \frac{64}{63}\frac{\Omega\lambda L^6 R^5}{\mu^5 b^4}\sigma_{xx}^4$$
$$P_2 = -\frac{A_3^H}{\left(A_2^H\right)^3} - \frac{16}{5}\frac{\Omega\lambda L^4 R^3}{\mu^3 b^2}\sigma_{xx} + \frac{256}{63}\frac{\Omega\lambda L^6 R^5}{\mu^5 b^4}\sigma_{xx}^3 \qquad \textit{(15)}$$
$$P_3 = -\frac{16}{5}\frac{\Omega\lambda\ {}^4 R^3}{\mu^3 b^2} + \frac{256}{21}\frac{\Omega\lambda L^6 R^5}{\mu^5 b^4}\sigma_{xx}^2$$

If the ultrasonic excitation are carried out perpendicular to the direction of the tensile load, this results in a multi-dimensional problem (Figure 4b). In this model, the longitudinal ultrasonic waves are sent perpendicularly (z-direction) to the vector of the tensile stress σ_{xx} causing plasticity. The sent longitudinal wave $u(z,t) = Acos[k(z-ct)]\begin{bmatrix}0\\0\\1\end{bmatrix}$ leads with $\varepsilon_{zz} = \frac{\partial u_z}{\partial z}$ to the isotropic linear elastic stress tensor $\sigma^u = -Aksin[k(z-ct)]\begin{bmatrix}\lambda & 0 & 0\\0 & \lambda & 0\\0 & 0 & \lambda+2\mu\end{bmatrix}$ [44], where u is the displacement, A is the amplitude, k is the wavenumber and c is the phase velocity. With λ = 109 GPa [45] and μ = 81 GPa [45], the lateral stresses (σ_{xx}^u and σ_{yy}^u) make up approximately 30% of the stress σ_{zz}^u. Due to the additional small entry area of the ultrasonic signal shown in Figure 4, Equation (7) is not influenced by the lateral components σ_{xx}^u and σ_{yy}^u because the entire body surface is significantly larger and ensures a rigid system, leading to the shown small stresses, which are significant lower in comparison to the mechanical stress σ_{xx} [46]. This allows a quasi-one-dimensional approach in the z-direction.

The stress change, $\Delta\sigma_{zz}^u$, due to the oscillatory ultrasonic signal, similarly leads Equation (12) to an additional strain $\Delta\varepsilon_{zz}$ (Equation (15)) [25]:

$$\Delta\sigma_{zz}^{u} = \frac{\partial\sigma_{xx}}{\partial\varepsilon_{zz}}\Delta\varepsilon_{zz}^{u} + \frac{1}{2}\frac{\partial^2\sigma_{xx}}{\partial{\varepsilon_{zz}}^2}(\Delta\varepsilon_{zz}^{u})^2 + \frac{1}{6}\frac{\partial^3\sigma_{xx}}{\partial{\varepsilon_{zz}}^3}(\Delta\varepsilon_{zz}^{u})^3 + \cdots. \tag{15}$$

The expression $\frac{\partial\sigma_{xx}}{\partial\varepsilon_{zz}}$ describes the plastic deformation ε_{zz} due to the tensile stress σ_{xx} and in the elastic deformation range it is the slope in the stress-strain diagram. According to Equation (13) the inverse function is:

$$\Delta\sigma_{zz}^{u} = \underbrace{\left(\frac{\partial\varepsilon_{zz}}{\partial\sigma_{xx}}\right)^{-1}}_{\alpha_d^{\perp}} \Delta\varepsilon_{zz}^{u} + \frac{1}{2}\underbrace{\left(-\frac{\partial^2\varepsilon_{zz}}{\partial{\sigma_{xx}}^2}\left(\frac{\partial\varepsilon_{zz}}{\partial\sigma_{xx}}\right)^{-3}\right)}_{\beta_d^{\perp}}(\Delta\varepsilon_{zz}^{u})^2 + \frac{1}{6}\underbrace{\left(-\frac{\partial^3\varepsilon_{zz}}{\partial{\sigma_{xx}}^3}\left(\frac{\partial\varepsilon_{zz}}{\partial\sigma_{xx}}\right)^{-4} + 3\left(\frac{\partial^2\varepsilon_{zz}}{\partial{\sigma_{xx}}^2}\right)^{2}\left(\frac{\partial\varepsilon_{zz}}{\partial\sigma_{xx}}\right)^{-5}\right)}_{\gamma_d^{\perp}}(\Delta\varepsilon_{zz}^{u})^3, \tag{16}$$

where $\alpha_d^{\perp}$is the first coefficient, $\beta_d^{\perp}$is the second-order nonlinearity coefficient, and $\gamma_d^{\perp}$is the third-order nonlinearity coefficient for the perpendicular ultrasonic excitation. Similar to Equation (13), Equation (16) is solved by inserting the ε_{zz}-component of Equation (11). When compared with Equation (16), the following relations result for the coefficients $\alpha_d^{\perp}$, $\beta_d^{\perp}$and $\gamma_d^{\perp}$:

$$\begin{gathered}
\alpha_d^{\perp} = \nu\left(-\frac{1}{A_2^H} - \frac{2}{3}\frac{\Omega\Lambda L^2 R}{\mu} + \frac{A_3^H}{(A_2^H)^3}\sigma_{xx} + \frac{8}{5}\frac{\Omega\Lambda L^4 R^3}{\mu^3 b^2}\sigma_{xx}^2 - \frac{64}{63}\frac{\Omega\Lambda L^6 R^5}{\mu^5 b^4}\sigma_{xx}^4\right)^{-1}, \\
\beta_d^{\perp} = \frac{-\frac{A_3^H}{\left(A_2^H\right)^3} - \frac{16}{5}\frac{\Omega\Lambda L^4 R^3}{\mu^3 b^2}\sigma_{xx} + \frac{256}{63}\frac{\Omega\Lambda L^6 R^5}{\mu^5 b^4}\sigma_{xx}^3}{\nu^2\left(-\frac{1}{A_2^H} - \frac{2}{3}\frac{\Omega\Lambda L^2 R}{\mu} + \frac{A_3^H}{\left(A_2^H\right)^3}\sigma_{xx} + \frac{8}{5}\frac{\Omega\Lambda L^4 R^3}{\mu^3 b^2}\sigma_{xx}^2 - \frac{64}{63}\frac{\Omega\Lambda L^6 R^5}{\mu^5 b^4}\sigma_{xx}^4\right)^3}, \\
\gamma_d^{\perp} = \frac{-\frac{16}{5}\frac{\Omega\Lambda L^4 R^3}{\mu^3 b^2} + \frac{256}{21}\frac{\Omega\Lambda L^6 R^5}{\mu^5 b^4}\sigma_{xx}^2}{\nu^3\left(-\frac{1}{A_2^H} - \frac{2}{3}\frac{\Omega\Lambda L^2 R}{\mu} + \frac{A_3^H}{\left(A_2^H\right)^3}\sigma_{xx} + \frac{8}{5}\frac{\Omega\Lambda L^4 R^3}{\mu^3 b^2}\sigma_{xx}^2 - \frac{64}{63}\frac{\Omega\Lambda L^6 R^5}{\mu^5 b^4}\sigma_{xx}^4\right)^4} + \frac{3\left(\frac{A_3^H}{\left(A_2^H\right)^3} + \frac{16}{5}\frac{\Omega\Lambda L^4 R^3}{\mu^3 b^2}\sigma_{xx} - \frac{256}{63}\frac{\Omega\Lambda L^6 R^5}{\mu^5 b^4}\sigma_{xx}^3\right)^2}{\nu^3\left(-\frac{1}{A_2^H} - \frac{2}{3}\frac{\Omega\Lambda L^2 R}{\mu} + \frac{A_3^H}{\left(A_2^H\right)^3}\sigma_{xx} + \frac{8}{5}\frac{\Omega\Lambda L^4 R^3}{\mu^3 b^2}\sigma_{xx}^2 - \frac{64}{63}\frac{\Omega\Lambda L^6 R^5}{\mu^5 b^4}\sigma_{xx}^4\right)^5}.
\end{gathered} \tag{17}$$

The behaviour of the nonlinearity coefficients $(\alpha_d, \beta_d$ and $\gamma_d)$ for both of the excitation directions are shown in Appendix B.

2.2. Dislocation and nonlinear modulation

The relationship between dislocations and nonlinearity coefficients were derived for the collinear model (||) and the orthogonal model (⊥). A quasi-one-dimensional wave propagation was assumed, and the nonlinearity coefficients α_d, $\beta_d$and γ_d were derived under an excitation with two frequencies. It was shown that the superposition of two fundamental waves offers accurate results in the determination of cracks [36, 37, 47].

The wave equation is: $\rho\frac{\partial^2 u}{\partial t^2} = \frac{\partial\sigma}{\partial s}$, where ρ is the mass density, u represents the displacement and s the wave propagation distance. The following derivations were made independently of the direction indicators and, therefore, the variable s is used instead of x and

z. The mass density ρ in the plasticized material is assumed to be constant over the wave propagation distance. With the definition of the nonlinearity coefficients up to the third-order (Equations (13) and (16)) this leads with [37] to the formulation of:

$$\frac{\partial^2 u}{\partial t^2} = \alpha_d c^2 \frac{\partial^2 u}{\partial s^2} + \beta_d c^2 \frac{\partial u}{\partial s}\frac{\partial^2 u}{\partial s^2} + \gamma_d \frac{c^2}{2}\left(\frac{\partial u}{\partial s}\right)^2 \frac{\partial^2 u}{\partial s^2}. \tag{18}$$

The assumption made for $u^{(1)}$ for dual-frequency excitation is:

$$u^{(1)} = A_1 sin\left[k_{f1}(s - ct)\right] + A_2 cos\left[k_{f2}(s - ct)\right]. \tag{20}$$

Equation (18) is solved in two steps. The perturbation method $(u(s,t) = u^{(1)} + u^{(2)} + u^{(3)} + \cdots)$ is used to find solutions for $u^{(2)}$ and $u^{(3)}$. The detailed derivation procedure is shown in [36, 37] and the accumulated solution of $u(s,t)$ is:

$$\begin{gathered}
u(s,t) = A_1 sin\left[k_{f1}(s - ct)\right] - \frac{\gamma_d}{\alpha_d}\frac{1}{8}\left(\frac{{A_1}^3{k_{f1}}^3}{2} + A_1{A_2}^2 k_{f1}{k_{f2}}^2\right) cos\left[k_{f1}(s - ct)\right]s \\
+A_2 cos\left[k_{f2}(s - ct)\right] + \frac{\gamma_d}{\alpha_d}\frac{1}{8}\left(\frac{{A_2}^3{k_{f2}}^3}{2} + {A_1}^2 A_2{k_{f1}}^2 k_{f2}\right) sin\left[k_{f2}(s - ct)\right]s \\
\frac{-\beta_d}{\alpha_d}\frac{A_1^2 k_{f1}^2}{8} cos\left[2k_{f1}(s - ct)\right]s \frac{+\beta_d}{\alpha_d}\frac{A_2^2 k_{f2}^2}{8} cos\left[2k_{f2}(s - ct)\right]s \\
\frac{-\gamma_d}{\alpha_d}\frac{1}{48}{A_1}^3{k_{f1}}^3 cos\left[3k_{f1}(s - ct)\right]s - \frac{\gamma_d}{\alpha_d}\frac{1}{48}{A_2}^3{k_{f2}}^3 sin\left[3k_{f2}(s - ct)\right]s \\
\frac{-\beta_d}{\alpha_d}\frac{A_1 A_2 k_{f1} k_{f2}}{4} sin\left[(k_{f2} - k_{f1})(s - ct)\right]s \\
\frac{+\beta_d}{\alpha_d}\frac{A_1 A_2 k_{f1} k_{f2}}{4} sin\left[(k_{f2} + k_{f1})(s - ct)\right]s \\
\frac{+\gamma_d}{\alpha_d}\frac{{A_1}^2 A_2}{8}\left(\frac{{k_{f1}}^2{k_{f2}}^2}{2(2k_{f1}+k_{f2})} + \frac{{k_{f1}}^3 k_{f2}}{2k_{f1}+k_{f2}}\right) sin\left[(2k_{f1} + k_{f2})(s - ct)\right]s \\
\frac{+\gamma_d}{\alpha_d}\frac{{A_1}^2 A_2}{8}\left(\frac{{k_{f1}}^2{k_{f2}}^2}{2(2k_{f1}-k_{f2})} - \frac{{k_{f1}}^3 k_{f2}}{2k_{f1}-k_{f2}}\right) sin\left[(2k_{f1} - k_{f2})(s - ct)\right]s \\
\frac{+\gamma_d}{\alpha_d}\frac{A_1{A_2}^2}{8}\left(\frac{{k_{f1}}^2{k_{f2}}^2}{2(2k_{f2}+k_{f1})} + \frac{k_{f1}{k_{f2}}^3}{2k_{f2}+k_{f1}}\right) cos\left[(2k_{f2} + k_{f1})(s - ct)\right]s \\
\frac{+\gamma_d}{\alpha_d}\frac{A_1{A_2}^2}{8}\left(\frac{-{k_{f1}}^2{k_{f2}}^2}{2(2k_{f2}-k_{f1})} + \frac{k_{f1}{k_{f2}}^3}{2k_{f2}-k_{f1}}\right) sin\left[(2k_{f2} - k_{f1})(s - ct)\right]s.
\end{gathered} \tag{19}$$

Equation (19) demonstrated the displacement components of the various harmonic frequencies and sidebands. The expressions also show that both fundamental frequencies $(A_{1,2}, k_{f1,2})$ are interdependent and that these are strongly influenced by the nonlinearity coefficients $(A_1 sin\left[k_{f1}(s - ct)\right] - \frac{\gamma_d}{\alpha_d} \ldots cos\left[k_{f1}(s - ct)\right]s$ and $A_2 cos\left[k_{f2}(s - ct)\right] + \frac{\gamma_d}{\alpha_d} \ldots sin\left[k_{f2}(s - ct)\right]s)$.

With an assumed constant wave propagation distance and wavenumber, the amplitude dependent nonlinearity parameters (Equation (20)) can be derived.

$$
\begin{aligned}
\left(\frac{\beta_d}{\alpha_d}\right)_{2f1} &\propto \frac{A_{f1+f2}}{{A_1}^2},\\
\left(\frac{\beta_d}{\alpha_d}\right)_{2f2} &\propto \frac{A_{f1+f2}}{{A_2}^2},\\
\left(\frac{\gamma_d}{\alpha_d}\right)_{3f1} &\propto \frac{A_{f1+f2}}{{A_1}^3},\\
\left(\frac{\gamma_d}{\alpha_d}\right)_{3f2} &\propto \frac{A_{f1+f2}}{{A_2}^3},\\
\left(\frac{\beta_d}{\alpha_d}\right)_{f2\pm f1} &\propto \frac{A_{f1+f2}}{A_1 A_2},\\
\left(\frac{\gamma_d}{\alpha_d}\right)_{2f1\pm f2} &\propto \frac{A_{f1+f2}}{{A_1}^2 A_2},\\
\left(\frac{\gamma_d}{\alpha_d}\right)_{2f2\pm f1} &\propto \frac{A_{f1+f2}}{A_1 {A_2}^2}.
\end{aligned}
\tag{20}
$$

Where the displacement u is interpreted as the accumulated amplitude of the harmonic or modulated response frequencies $\left(u(s,t) = A_{f1+f2}\right)$ [36, 37, 47]. This leads to direct conclusions about the amplitudes of the harmonic frequencies and modulated response frequencies. The derived equations show the various nonlinearity parameters as a function of the material, dislocation, frequency-characteristics and the applied tensile stress. For the evaluation of the nonlinearity parameters, the ratios $\frac{\beta_d}{\alpha_d}$ and $\frac{\gamma_d}{\alpha_d}$ are described with the parameter δ.

2.3. Nonlinearity behaviour

The behaviour of the nonlinearity parameters with increasing plastic strain was modelled using data from literature. The physical values for cold rolled stainless steel (304 SS / 1.4301) are summarized in Table 1.

Table 1. Physical parameters – dislocation simulation.

Physical parameters		**Reference**	**Load steps**				
			1	2	3	4	5
Applied Stress σ [MPa]		[48]	235	443	673	887	1113
Dislocation density Λ [$\times 10^{14}$ m^{-2}]		[48]	0.67	3.05	4.48	4.82	5.59
Dislocation length L [nm]		[48]	23				
Burgers vector b [nm]		[48]	2.5				
Lamé constants (2nd order) [GPa]	λ [GPa]	[45]	109				
	μ [GPa]	[45]	81.7				
Murnaghan constants (3rd order) [GPa]	l [GPa]	[45]	–671				
	m [GPa]	[45]	–56				
Huang coefficients [GPa]	A_2^H [GPa]	Equation (9)	272.4				
	A_3^H [GPa]	Equation (10)	–1978.8				
Conversion factor Ω		[32, 49]	0.33				
Schmid factor R		[32, 49]	0.33				
Poisson's ratio v		[32, 49]	0.3				

It was assumed that the shear modulus or Lamé constant, μ, after the deformation also remains at the same value as before the deformation [50].

The fundamental frequencies f_1 = 6 MHz and f_2 = 10 MHz were used for the two-frequency excitation; this is in line with the experimental testing reported in Section 3. A phase velocity of c = 5820 m/s was used for the defined material with the wave numbers $k_{f1,2} = \frac{f_{1,2}}{c}$.

It was demonstrated that the various nonlinearity parameters behave differently with increasing plastic strains. Some nonlinearity parameters increase in values, while others decrease. If the resulting parallel and orthogonal excited nonlinearity parameters are compared, the behaviour illustrated differences. It was shown whether the nonlinearity parameters increase (+) and decrease (–) with increasing plastic strain (Table 2). It is also indicated which degree of nonlinearity leads to these results. All (β_d/α_d)-dependent nonlinearity parameters change the behaviour depending on the ultrasonic excitation vector. In a sensitivity study, it was shown that

Poisson's ratio had a major impact on the results. In the parallel perspective in Figure 5, the nonlinearity parameter $\delta 2f_1$ increases with increasing plastic deformation. The parameter $\delta 2f_2$, however, decreases. The nonlinearity parameters of the third harmonic frequencies $\delta 3f_{1,2}$ even drop both. With the modulated response frequencies, the opposite behaviour continues. The nonlinearity parameters δf_2+f_1 decrease with increasing plastic strain, while type δf_2-f_1

increase. Figure 5d,e show that the nonlinearity parameters $\delta 2f_1 – f_2$ and $\delta 2f_2 – f_1$ increase with increasing strain, while the parameters $\delta 2f_1 + f_2$ and $\delta 2f_2 + f_1$ decrease.

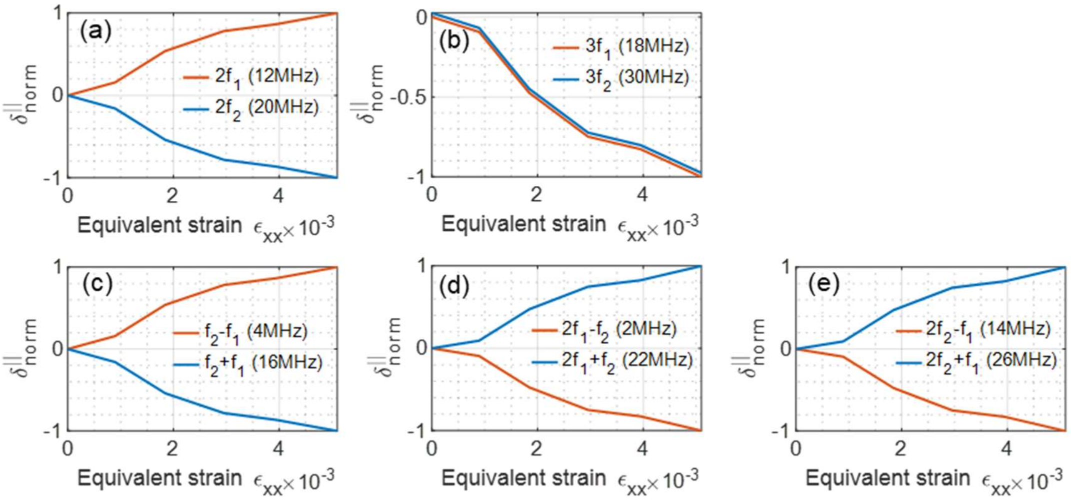

Figure 5. Dislocation behaviour – collinear excitation: (a) $\delta 2f_{1,2}$; (b) $\delta 3f_{1,2}$; (c) $\delta f_2 \pm f_1$; (d) $\delta 2f_1 \pm f_2$; (e) $\delta 2f_2 \pm f_1$.

In the orthogonal ultrasonic excitation, on the other hand (Figure 6), the parameter $\delta 2f_2$ increases with increasing plastic deformation and $\delta 2f_1$ decreases. The other difference is given with the modulated response parameters $\delta f_2 \pm f_1$. With $\delta f_2 + f_1$ the nonlinearity values increase while with parameter $\delta f_2 - f_1$ they decrease. The parameters of the modulated response frequencies of higher order behave exactly as with the parallel excitation.

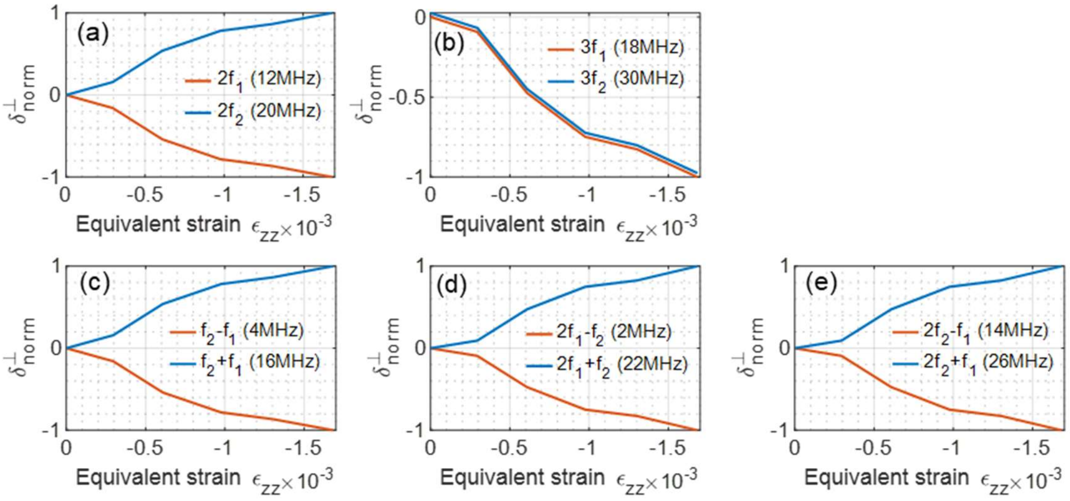

Figure 6. Dislocation behaviour – orthogonal excitation: (a) $\delta 2f_{1,2}$; (b) $\delta 3f_{1,2}$; (c) $\delta f_2 \pm f_1$; (d) $\delta 2f_1 \pm f_2$; (e) $\delta 2f_2 \pm f_1$.

Table 2. Behaviour collinear and orthogonal nonlinearity parameter.

Frequency	**Nonlinearity coefficients**	**Behaviour nonlinearity parameter** [1]	
	$\left(\frac{\beta_d}{\alpha_d}\right), \left(\frac{\gamma_d}{\alpha_d}\right)$	**Collinear ultrasonic excitation** (∥)	**Orthogonal ultrasonic excitation** (⊥)
$2f_1$	$\left(\frac{\beta_d}{\alpha_d}\right)$	+	–
$2f_2$	$\left(\frac{\beta_d}{\alpha_d}\right)$	–	+
$3f_1$	$\left(\frac{\gamma_d}{\alpha_d}\right)$	–	–
$3f_2$	$\left(\frac{\gamma_d}{\alpha_d}\right)$	–	–
f_2-f_1	$\left(\frac{\beta_d}{\alpha_d}\right)$	+	–
f_2+f_1	$\left(\frac{\beta_d}{\alpha_d}\right)$	–	+
$2f_1$-f_2	$\left(\frac{\gamma_d}{\alpha_d}\right)$	–	–
$2f_1$+f_2	$\left(\frac{\gamma_d}{\alpha_d}\right)$	+	+
$2f_2$-f_1	$\left(\frac{\gamma_d}{\alpha_d}\right)$	–	–
$2f_2$+f_1	$\left(\frac{\gamma_d}{\alpha_d}\right)$	+	+

[1] '+' means an increasing nonlinearity parameter with increasing plasticisation.
'–' means a decreasing nonlinearity parameter with increasing plasticisation.

Table 2 summarizes the behaviour of the nonlinearity parameters for the different ultrasonic excitation directions. The dual-frequency excitation with increasing nonlinearity parameters was successfully used to detect cracks [36, 37], where an increase for all nonlinearity parameters was found in the damaged samples.

3. Experimental results

In the previous section, the one-dimensional wave equation with dual-frequency excitation was combined with the dislocation theory. The validation of the theoretical derivation of the nonlinearity parameters was carried out experimentally in this section.

3.1. Nonlinear ultrasonic behaviour with orthogonal excitation (⊥)

Three different materials were investigated experimentally. Sample were made of stainless steel (1.4571) and Inconel 718 (plate and SLM) respectively. The samples were prepared according to the standard for tensile tests ISO 6892 (Figure 7).

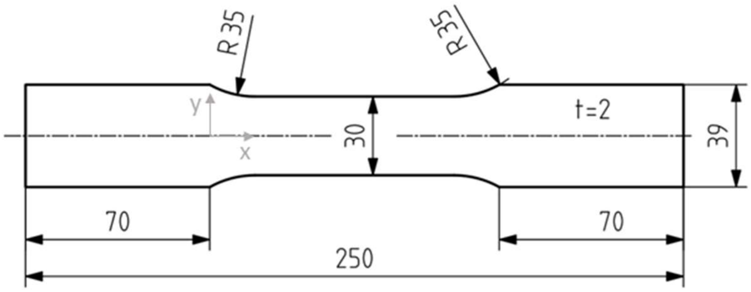

Figure 7. Dimensions flat tensile specimen.

To obtain points of reference for the plastic strain measurements, the yield strengths of the samples were determined experimentally. The measurements were repeated a total of five times and the arithmetic mean was calculated for the stress-strain curve. Figure 8 shows the samples after the tensile test.

Figure 8. Specimen tensile test: (a) stainless steel (1.4571); (b) Inconel 718 (Plate); (c) Inconel 718 (SLM).

Figure 9 reports the stress-strain diagram of the samples. After manufacturing, the samples produced by SLM were subjected to a heat treatment in the form of a precipitation hardening, which leads to an increase in strength.

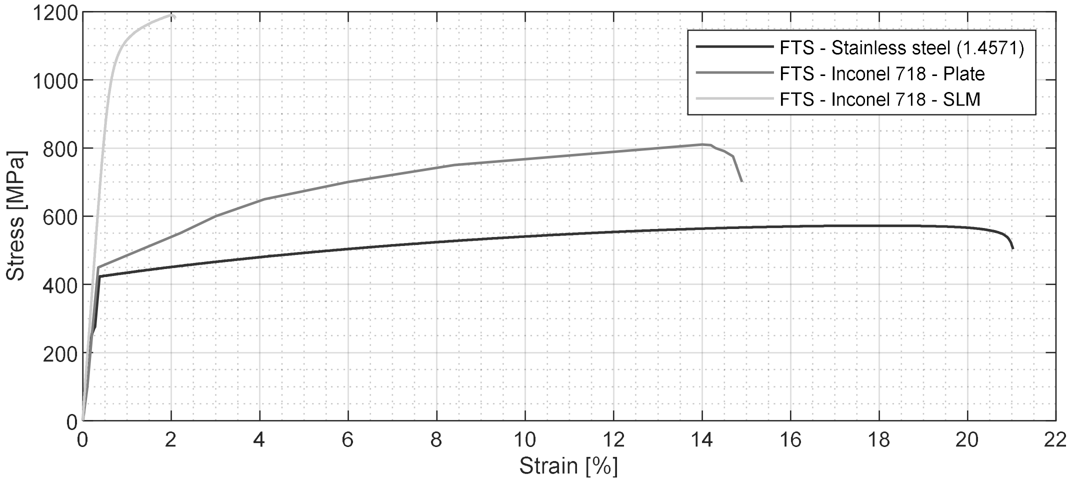

Figure 9. Stress-strain diagram.

Table 3 summarizes the determined material parameters (yield strength ($R_{p0.2}$), tensile strength (R_m) and elongation at break (A)).

Table 3. Mechanical properties – tensile test.

Specimen	Material	$R_{p0.2}$ [MPa]	R_m [MPa]	A [%]
FTS_A4_01–05	1.4571	304	572	48.5
FTS_IN718_01–05	Inconel 718 – Plate	494	816	34.1
FTS_SLM_IN718_01–05	Inconel 718 – SLM	1076,5	1174	12.4

Samples were loaded with a tensile testing machine up to the plastic deformation area (Figure 10). Table 4 shows the summary of the generated plastic strains. For the stainless steel sample (1.4571), a total of six different plastic strain states were generated, for the Inconel 718 plate five samples were produced and for the SLM-manufactured Inconel 718 samples, only three different strain variants were made available.

Figure 10. Sample plasticisation.

Table 4. Samples – plastic strains.

Sample No.	Plastic strain [%]		
	Stainless steel – 1.4571	Inconel 718 – Plate	Inconel 718 – SLM
1	2.6	1.8	1.2
2	3.2	3.2	1.6
3	3.4	3.6	2.4
4	4.0	6.0	–
5	4.8	6.4	–
6	5.6	–	–

The plasticized samples were examined by ultrasound. For this purpose, longitudinal waves with frequencies $f_1 = 6$ MHz and $f_2 = 10$ MHz were sent into the components using the Olympus V129–SM sensor with an active element diameter of 5 mm. The signals on the other side of the samples were received with the same type sensor. The pulse generator Rigol DG1022Z generated the signals and forwarded them to the high-voltage amplifier Falco Systems WMA–300 and amplified them to 150 V. The received signal was amplified with the Phoenix ISL 40 dB amplifier and sent to the Picoscope 5243 oscilloscope for post-processing (Figure 11).

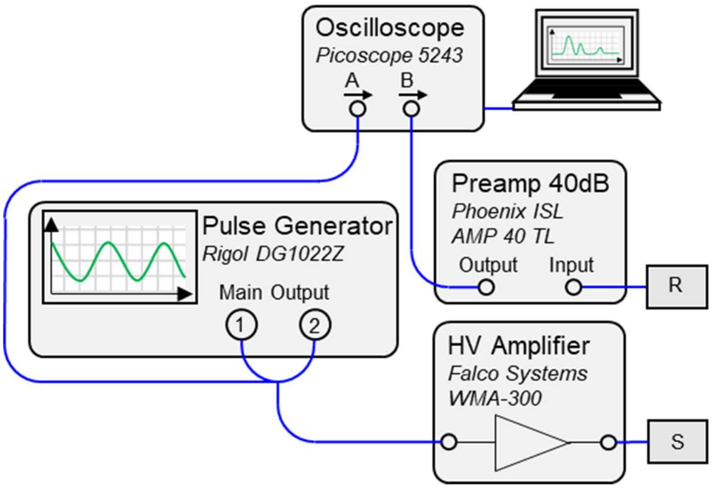

Figure 11. Experimental setup – scheme.

The measurements were carried out in the middle of the samples at 13 points (Figure 12a). Points 1 and 13 were in the sample width of 39 mm and points 2 and 12 were in the area of the transition radius. All other points were in the main measuring range of the sample thickness of 30 mm. This allows the weakest point in the sample to be identified.

The sensors were held in position with an additively manufactured sensor holder and ensures a constant preload from sensor to sample for each measurement (Figure 12b). Contact gel was used to improve signal transmission and the measurements at each point were repeated ten times.

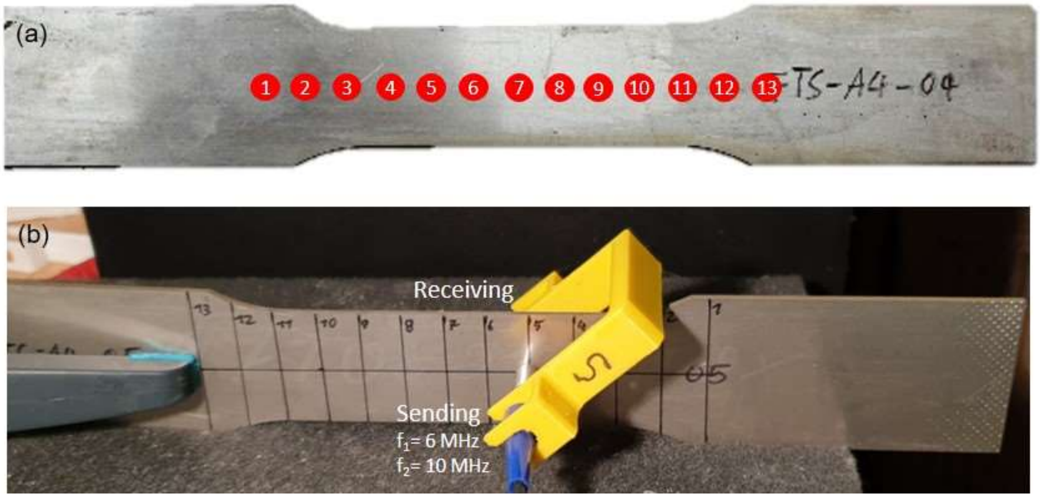

Figure 12. Experiments: (a) measuring positions; (b) experimental setup.

The average values of the amplitudes of the fundamental, harmonic and modulated response frequencies were determined, and the nonlinearity parameters were calculated using Equation **Error! Reference source not found.**).

Due to the plastic deformation, the thicknesses of the samples were reduced up to 0.1 mm. Equation (19) illustrated a linear behaviour of the displacement *u* as a function of the wave propagation distance *z* (*s*) (Figure 13), where the section relevant for the following experiments is marked in red. In these cases, the influence of the component thicknesses on the measured amplitudes can be neglected.

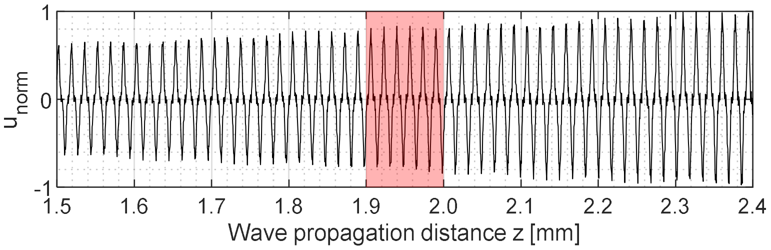

Figure 13. Influence – wave propagation distance.

3.1.1. Stainless steel samples

Figure 14 to Figure 18 show the various nonlinearity parameters for the individual measuring points. The measurement results of the reference sample with $\varepsilon = 0\%$ are always shown with a red line. Since the measuring points 1, 2 and 12, 13 are not in the narrower cross-section of the sample, the areas are greyed out and only viewed indirectly. How the nonlinearity parameters changed from these points to the actual measuring range was observed. This is also an indication of the inhomogeneous plastic deformation in the component.

Starting from the reference sample, the values of the nonlinearity parameters $\delta 2f_l$ decrease (Figure 14a). The minimum values are achieved by the sample with the highest strain ($\varepsilon = 5.6\%$). The parameter $\delta 2f_2$ (Figure 14b) demonstrates the opposite behaviour. A clear increase in the nonlinearity parameters of the plastically deformed samples were observed.

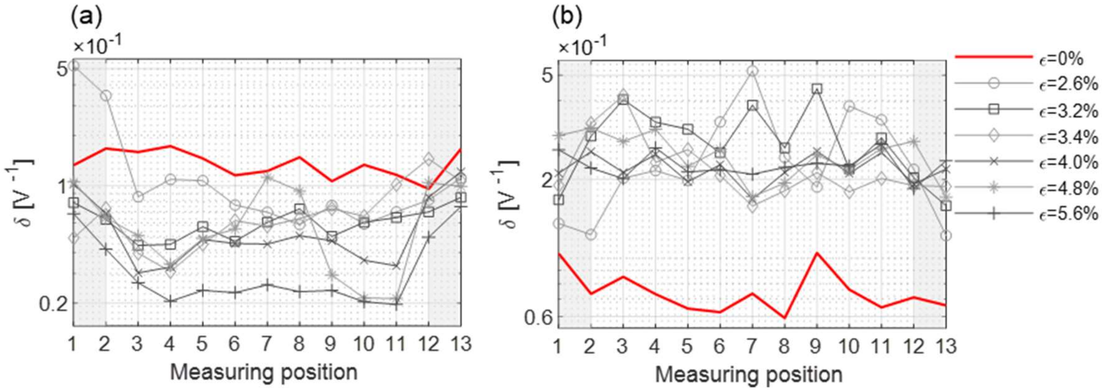

Figure 14. Nonlinearity parameters – stainless steel: (a) δ2f₁; (b) δ2f₂.

Figure 15 reveals the behaviour of the third harmonic frequencies 3f₁,₂. The parameter values show a decaying behaviour for both harmonics. The change in points 1 and 13 is particularly noticeable. Since the degree of plasticization is not as high as at measuring points 3 to 11, these are only slightly lower than the reference sample. From sample ε = 5.6%, the plasticization is not constantly distributed. With higher plastic strains, the weakest points were identified at the measuring points 4 and 11 (Figure 15b).

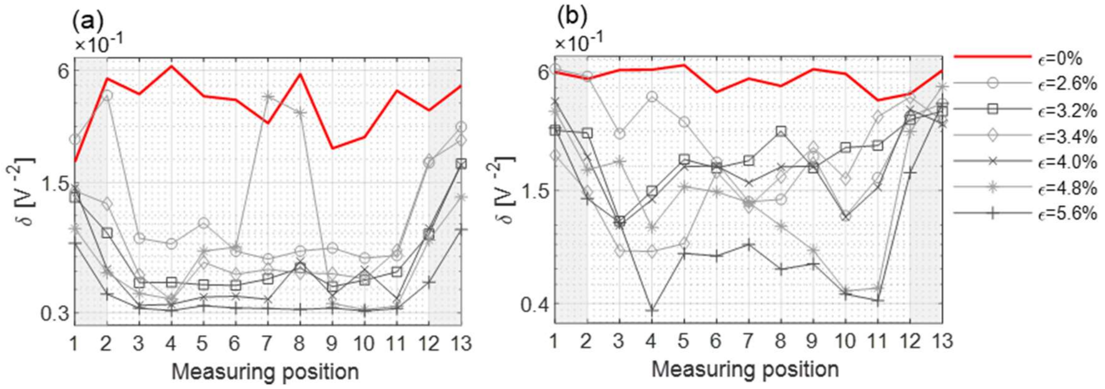

Figure 15. Nonlinearity parameters – stainless steel: (a) δ3f₁; (b) δ3f₂.

In Figure 16 the first modulated response frequencies and their nonlinearity parameters are shown. As observed before, an opposite behaviour is revealed. While the parameter δf₂–f₁ values decrease (Figure 16a), at δf₂+f₁ they increase with increasing plastic strain (Figure 16b).

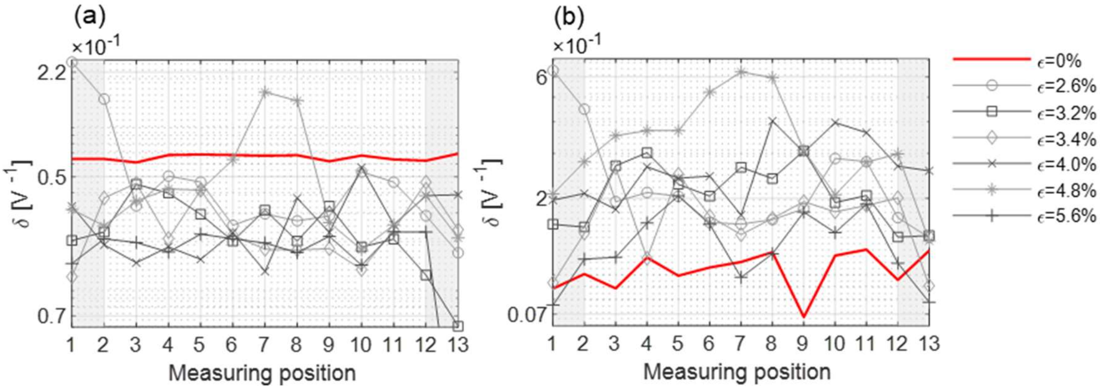

Figure 16. Nonlinearity parameters – stainless steel: (a) $\delta f_2 – f_1$; (b) $\delta f_2 + f_1$.

Figure 17 and Figure 18 demonstrate the modulated response parameters $\delta 2f_1 \pm f_2$ and $\delta 2f_2 \pm f_1$. The behaviour reveals that the $\delta 2f_1 – f_2$ / $\delta 2f_2 – f_1$ values decrease and the $\delta 2f_1 + f_2$ / $\delta 2f_2 + f_1$ values increase with increasing plasticization. Especially with the parameters $\delta 2f_1 – f_2$ (Figure 17a) and $\delta 2f_2 – f_1$ (Figure 18a), the weakest points of the $\varepsilon = 5.6\%$ sample are in position 4 and 11.

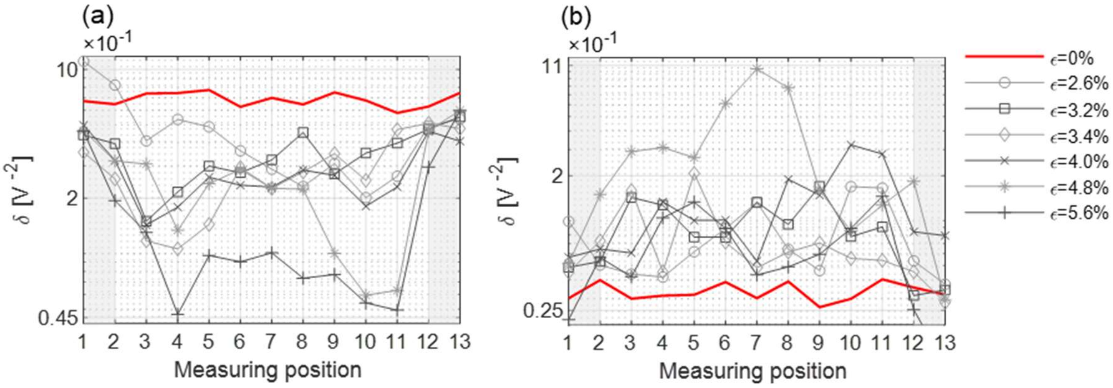

Figure 17. Nonlinearity parameters – stainless steel: (a) $\delta 2f_1 – f_2$; (b) $\delta 2f_2 + f_1$.

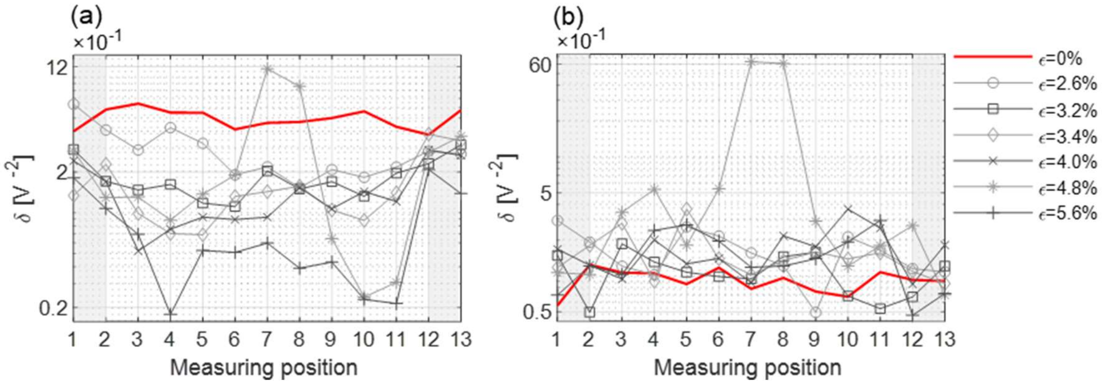

Figure 18. Nonlinearity parameters – stainless steel: (a) $\delta 2f_2 – f_1$; (b) $\delta 2f_2 + f_1$.

To summarize the results of the Figure 14 to Figure 18, the extreme values between points 3 to 11 were evaluated depending on their increasing or decreasing behaviour. With reference to the theoretical behaviour (Section 2), the minimum values were evaluated for the decreasing nonlinearity parameters $2f_1$, f_2+f_1, $2f_1+f_2$ and $2f_2+f_1$ and for the increasing parameters $2f_2$, $3f_1$, $3f_2$, f_2-f_1, $2f_1-f_2$ and $2f_2-f_1$, the maximum values for the points 3 to 11 were evaluated. This means that the weakest points in terms of plastic strain can be identified through the plot of nonlinear parameters. Figure 19 reveals the normalised results for all harmonic and modulated response frequencies. The behaviour of the various parameters becomes clear with increasing plasticity and agrees with the analytically behaviour (Table 2). The behaviour of the nonlinearity parameters are reported with increasing plastic strain from the reference sample to the most deformed sample.

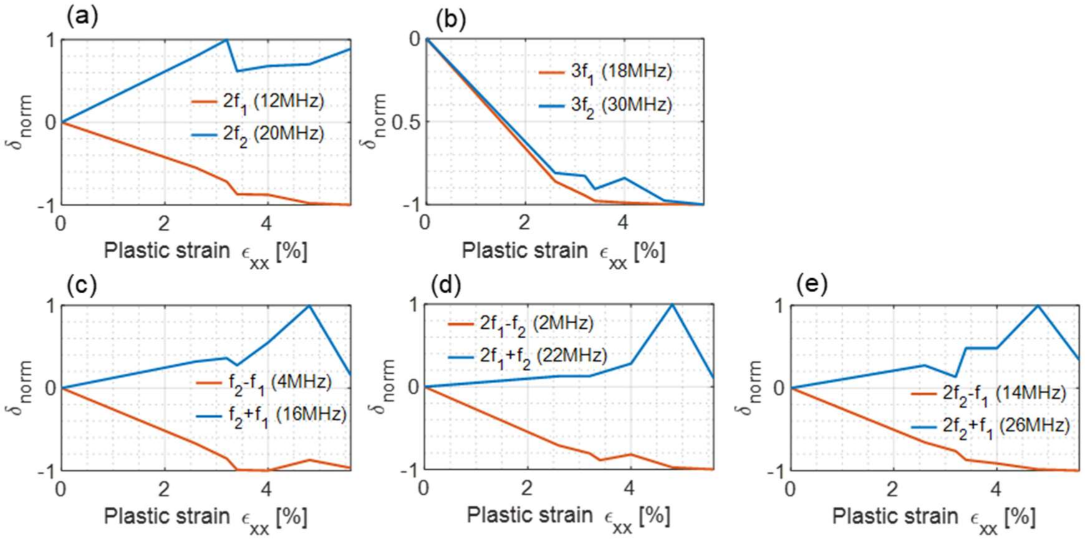

Figure 19. Stainless steel – dislocation behaviour: (a) $\delta 2f_{1,2}$; (b) $\delta 3f_{1,2}$; (c) $\delta f_2 \pm f_1$; (d) $\delta 2f_1 \pm f_2$; (e) $\delta 2f_2 \pm f_1$.

3.1.2. Inconel 718 – plate samples

Figure 20 to Figure 24 shows the measurement results of the Inconel 718 samples made of plate material. The harmonic frequencies $2f_1$ (Figure 20a) and $2f_2$ (Figure 20b) reveal opposite behaviour. The third harmonic frequencies $3f_{1,2}$, shown in Figure 21, both decrease with increasing plastic strain.

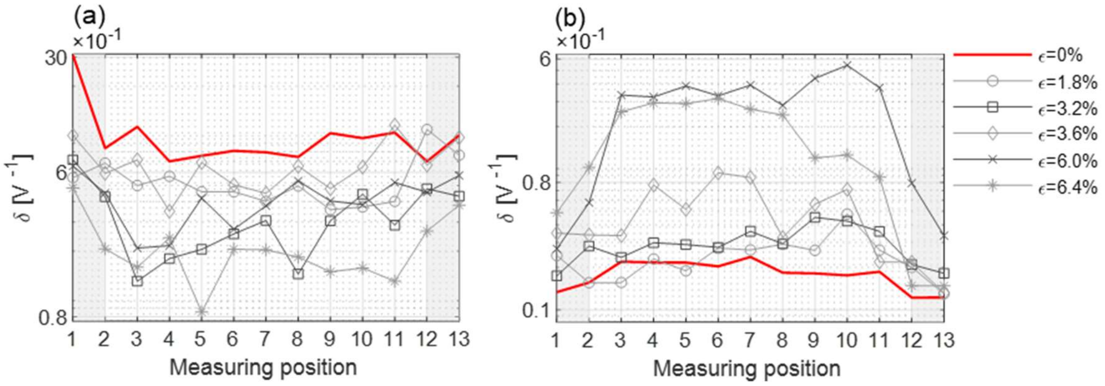

Figure 20. Nonlinearity parameters – Inconel 718: (a) $\delta 2f_1$; (b) $\delta 2f_2$.

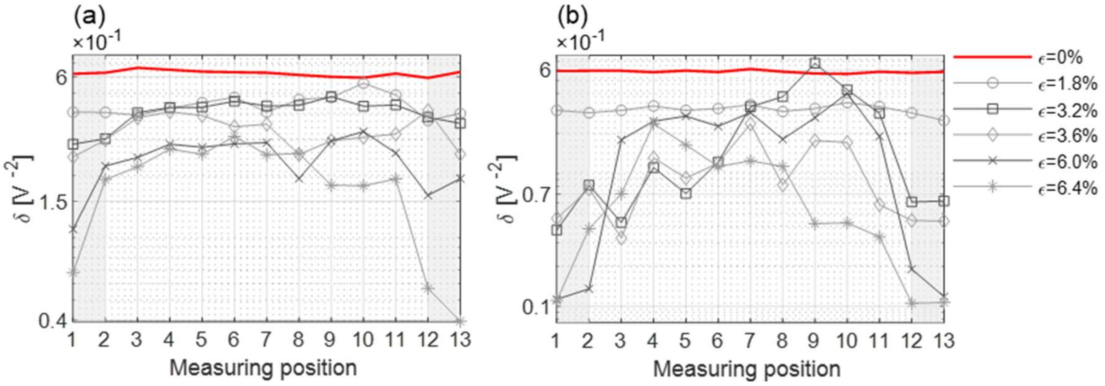

Figure 21. Nonlinearity parameters – Inconel 718: (a) $\delta 3f_1$; (b) $\delta 3f_2$.

The measurement results of the modulated response frequencies are shown in Figure 22 to Figure 24. As with the stainless steel samples, the group parameters $f_2 \pm f_1$ behave in opposite directions. With types $\delta f_2 - f_1$, $\delta 2f_1 - f_2$ and $\delta 2f_2 - f_1$ the nonlinearity parameters decrease with increasing plastic strain (Figure 22a, Figure 23a and Figure 24a) and with $\delta f_2 + f_1$, $\delta 2f_1 + f_2$ and $\delta 2f_2 + f_1$ they increase (Figure 22b, Figure 23b and Figure 24b). The weakest positions can be identified, particularly for the samples with higher plastic strain.

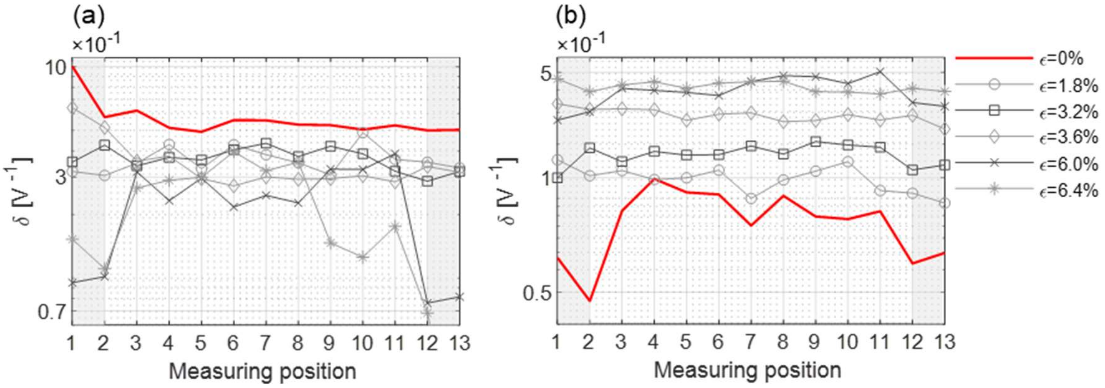

Figure 22. Nonlinearity parameters – Inconel 718: (a) $\delta f_2 – f_1$; (b) $\delta f_2 + f_1$.

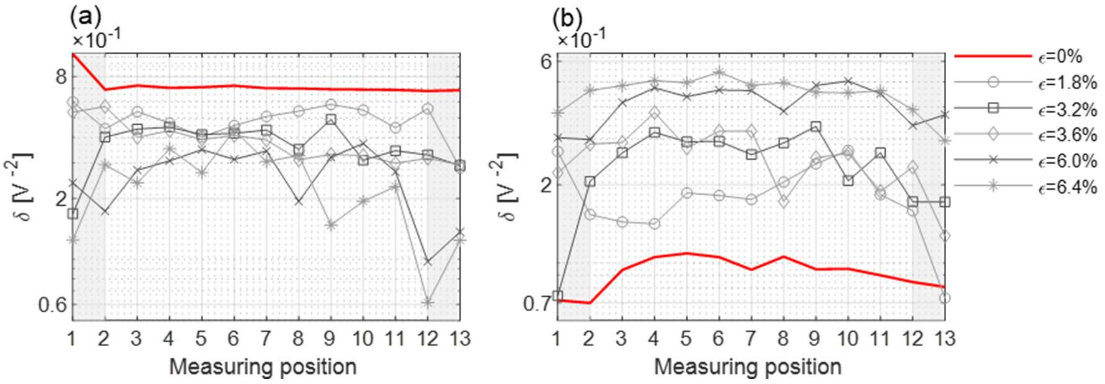

Figure 23. Nonlinearity parameters – Inconel 718: (a) $\delta 2f_1 – f_2$; (b) $\delta 2f_2 + f_1$.

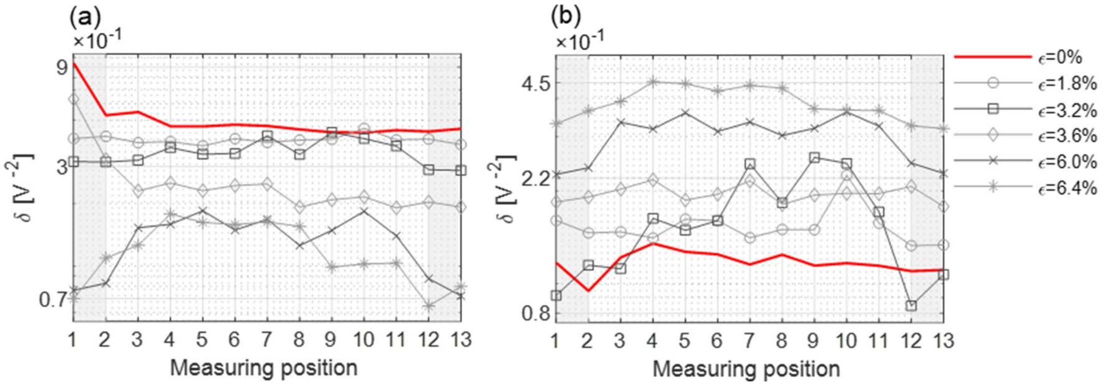

Figure 24. Nonlinearity parameters – Inconel 718: (a) $\delta 2f_2 – f_1$; (b) $\delta 2f_2 + f_1$.

Figure 25 summarises the behaviour of the nonlinearity parameters and the various samples through the extreme values of points 3 to 11. With small exceptions (Sample $\varepsilon = 4.6\%$ / 6.0% in Figure 25b), the mean values correspond to the results of the stainless steel samples and the analytical predictions. The variation coefficient of the values is a maximum of 4.5%.

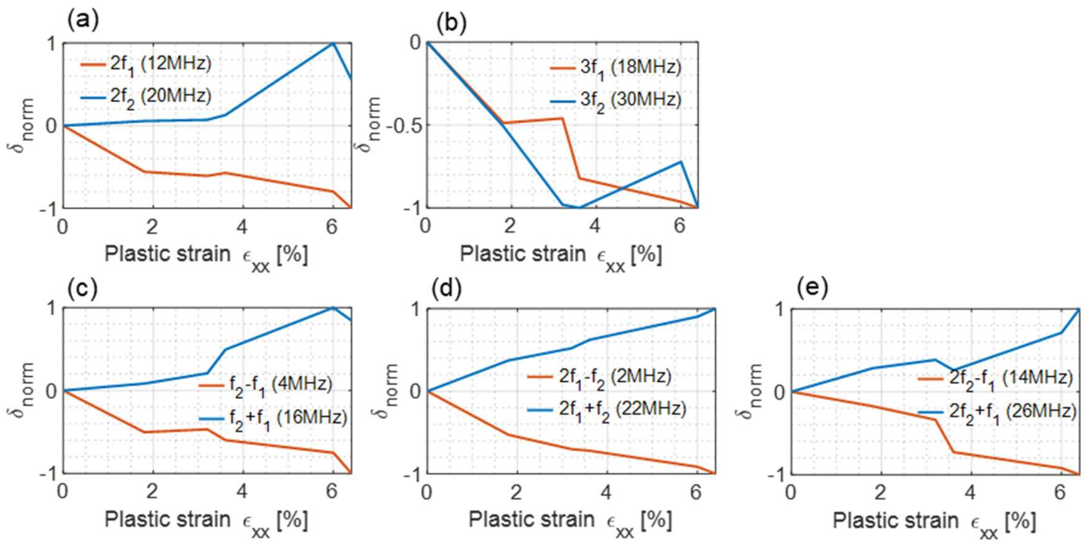

Figure 25. Inconel 718 plate – dislocation behaviour: (a) $\delta 2f_{1,2}$; (b) $\delta 3f_{1,2}$; (c) $\delta f_2 \pm f_1$; (d) $\delta 2f_1 \pm f_2$; (e) $\delta 2f_2 \pm f_1$.

3.1.3. Inconel 718 – SLM samples

The nonlinear results of the Inconel 718 samples manufactured by SLM are discussed below. In Figure 26a the decreasing behaviour of the harmonic frequency $2f_1$ is shown. The values increase at $2f_2$ (Figure 26b). The sample $\varepsilon = 1.6\%$ revealed peak values at points 4 and 9, where the highest degrees of plasticization were assumed. The parameters at the third harmonic frequencies $3f_{1,2}$ both decrease again with increasing plasticization (Figure 27).

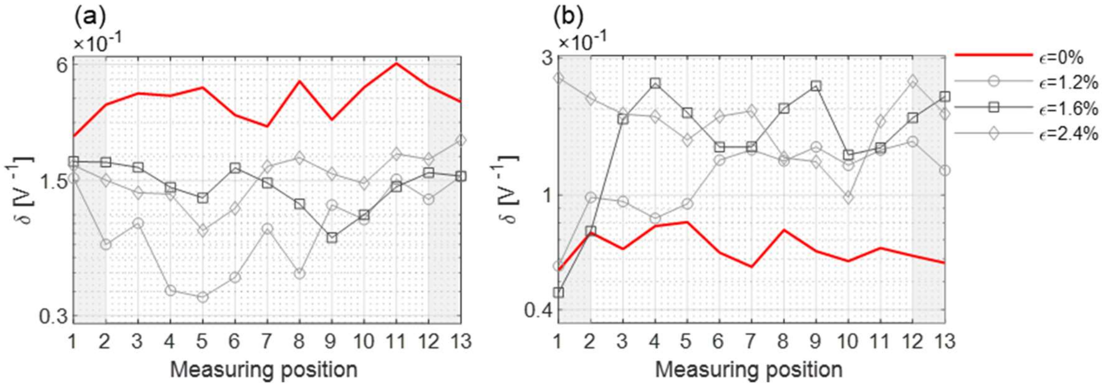

Figure 26. Nonlinearity parameters – Inconel 718 – SLM: (a) $\delta 2f_1$; (b) $\delta 2f_2$.

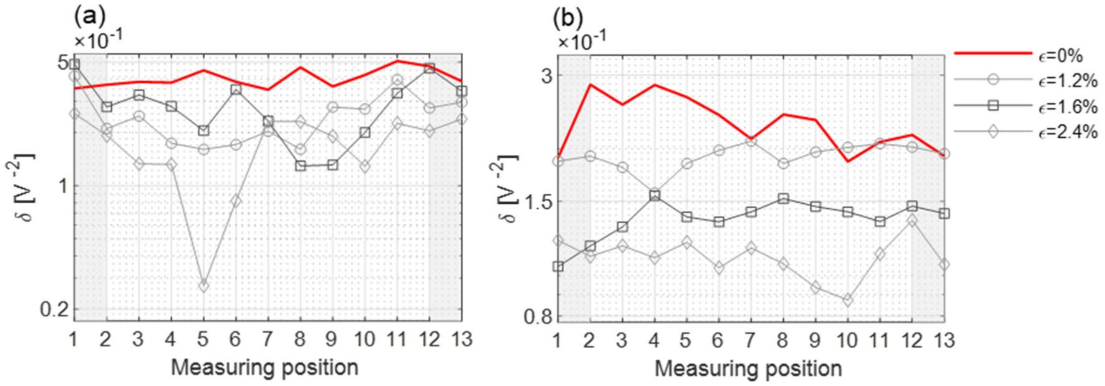

Figure 27. Nonlinearity parameters – Inconel 718 – SLM: (a) $\delta 3f_1$; (b) $\delta 3f_2$.

As with the other samples, the modulated response frequencies show opposing behaviours. With types $\delta f_2–f_1$, $\delta 2f_1–f_2$ and $\delta 2f_2–f_1$ (Figure 28a, Figure 29a and Figure 30a), the nonlinearity parameters decrease while they increase with δf_2+f_1, $\delta 2f_1+f_2$ and $\delta 2f_2+f_1$ (Figure 28b, Figure 29b and Figure 30b).

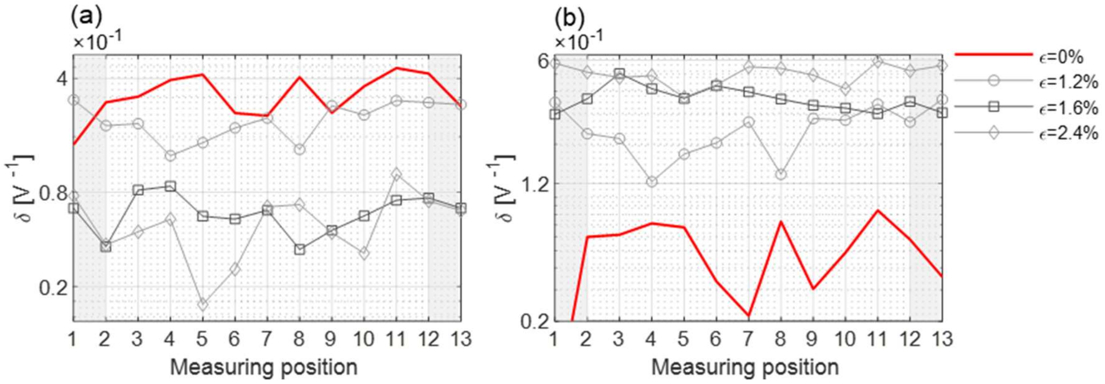

Figure 28. Nonlinearity parameters – Inconel 718 – SLM: (a) $\delta f_2–f_1$; (b) δf_2+f_1.

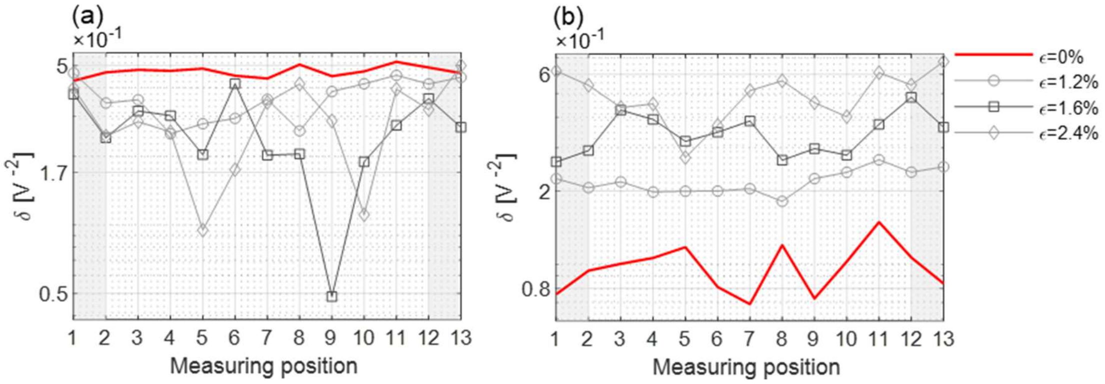

Figure 29. Nonlinearity parameters – Inconel 718 – SLM: (a) $\delta 2f_1–f_2$; (b) $\delta 2f_2+f_1$.

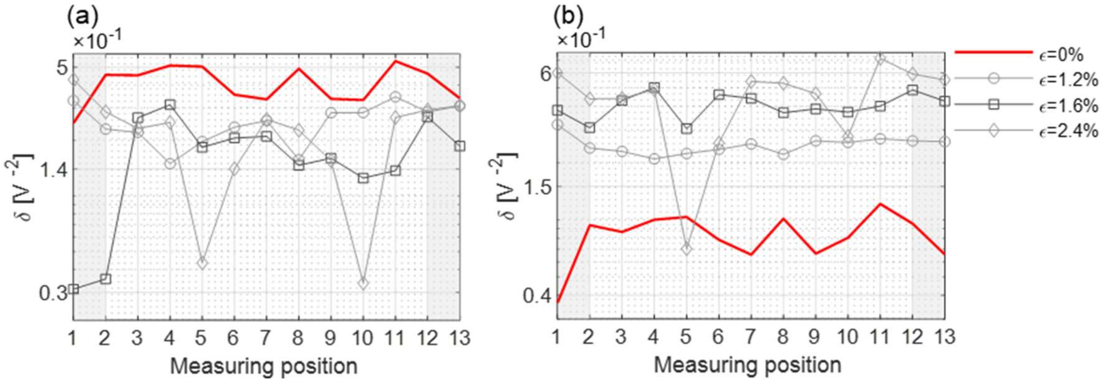

Figure 30. Nonlinearity parameters – Inconel 718 – SLM: (a) $\delta 2f_2–f_1$; (b) $\delta 2f_2+f_1$.

In summary, Figure 31 reveals an overview of the evaluation of the extreme values for the SLM manufactured samples. The majority of these values showed the same behaviour with the stainless steel and Inconel 718 plate samples and the analytical derivations. Only for the frequencies $2f_1$, $2f_2$, a monotonic increasing or decreasing behaviour was not observed, however, the trend shows higher nonlinearities when compared with the reference sample. The variation coefficient of the values is a maximum of 4.2%.

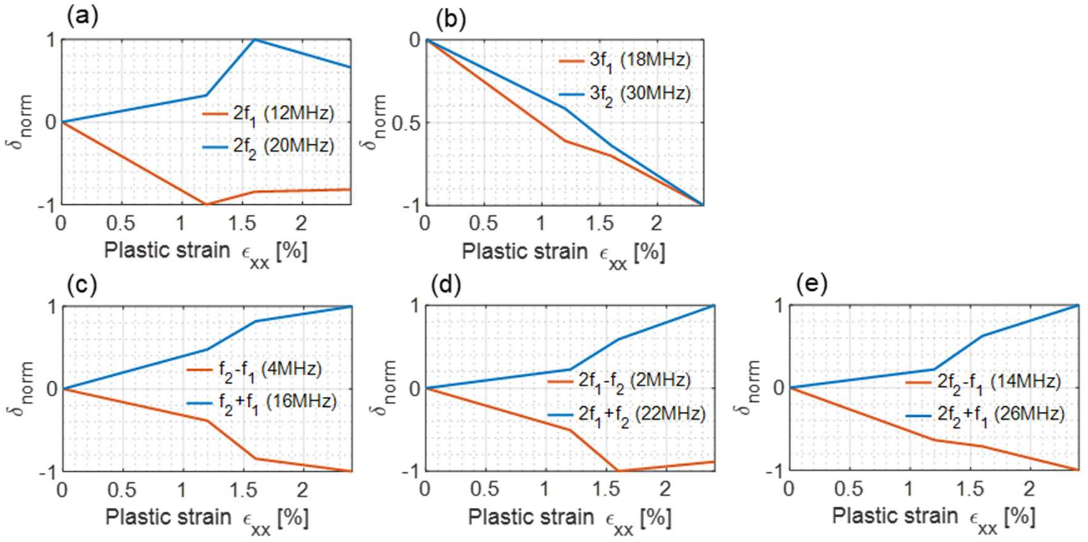

Figure 31. Inconel 718 SLM – dislocation behaviour: (a) $\delta 2f_{1,2}$; (b) $\delta 3f_{1,2}$; (c) $\delta f_2 \pm f_1$; (d) $\delta 2f_1 \pm f_2$; (e) $\delta 2f_2 \pm f_1$.

3.2. Comparison – nonlinear ultrasonic behaviour of collinear (∥) and orthogonal excitation (⊥)

In Section 3.1 the theoretical behaviour was proven experimentally, where the ultrasonic signal was applied perpendicularly to the tensile load.

The differences shown in Section 2.3 with the opposite behaviour depending on the direction of the ultrasonic excitation were also investigated experimentally. To provide the sensors a sufficient surface for sending the ultrasonic signals, aluminium samples made of AlMgSi1 were loaded with a tensile stress of $\sigma_{xx} = 270$ MPa to generate plastic deformations. The reference samples were compared with the plasticized samples in the various measuring directions (∥ and ⊥ in Figure 32). Five reference samples and five plasticized samples were available. The measurements of each sample were repeated ten times and the average was calculated.

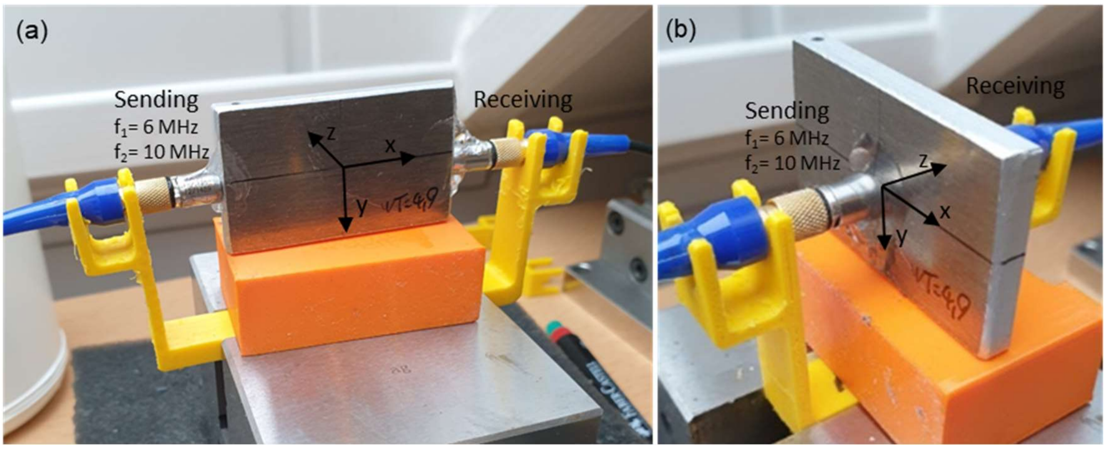

Figure 32. Experimental setup: (a) collinear excitation, ∥; (b) orthogonal excitation, ⊥.

The results of the various nonlinearity parameters with the measurement directions are shown in Figure 33. With $\delta 2f_{1,2}$ (Figure 33a) and $\delta f_2 \pm f_1$ (Figure 33c), the difference between ∥ and ⊥ becomes clear because the behaviour is reversed with the $\frac{\beta_d}{\alpha_d}$-dependent parameters. As already analytically predicted, the behaviour of the $\frac{\gamma_d}{\alpha_d}$ parameters behave in the same way. With $\delta 3f_{1,2}$ (Figure 33b), $\delta 2f_1 \pm f_2$ (Figure 33d) and $\delta 2f_2 \pm f_1$ (Figure 33e) do not reveal a different tendency from ⊥ to ∥.

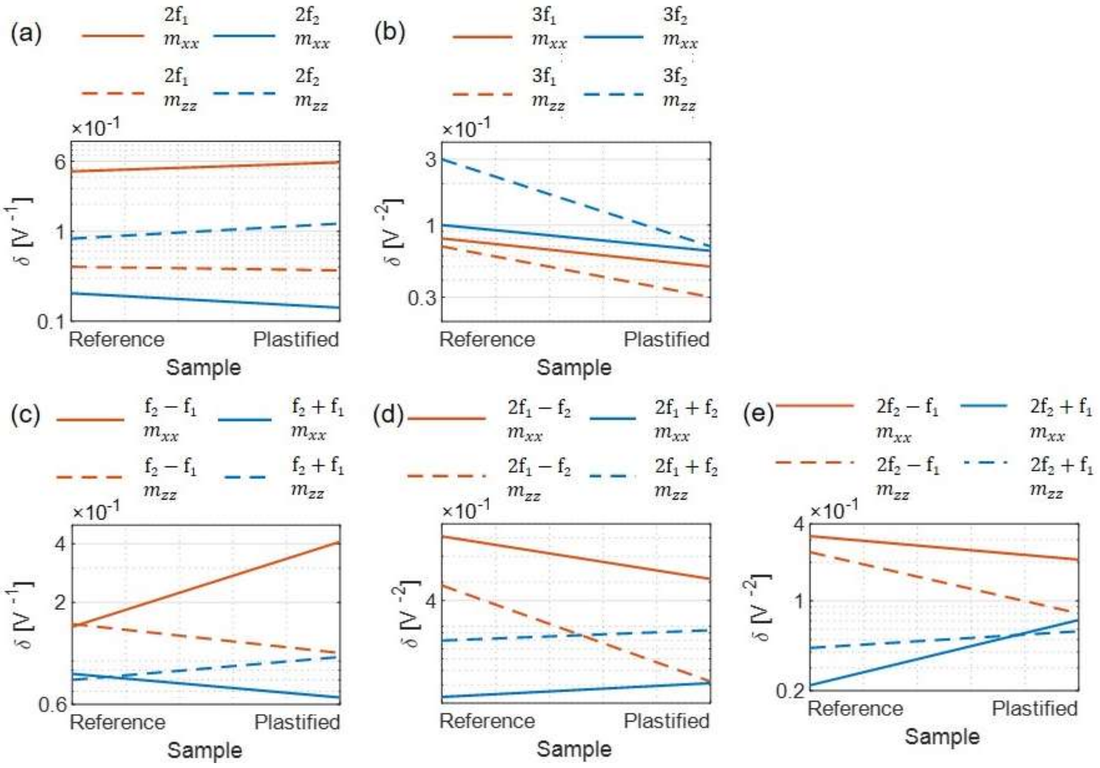

Figure 33. Nonlinearity parameters – comparison ∥ and ⊥: (a) $2f_{1/2}$; (b) $3f_{1/2}$; (c) $f_2 \pm f_1$; (d) $2f_1 \pm f_2$; (e) $2f_2 \pm f_1$.

The investigations explicated in this section illustrate that the mechanical load direction relative to the ultrasonic measurement can be determined based on the behaviour of the nonlinearity parameters and proved the analytical results shown in Table 2.

The measurements, evaluations and interpretations shown above are only valid if non-dispersive wave components were formed from the sent longitudinal waves. Since the sensors in Figure 32a are placed very close to the edge of the sample, other waveforms can be created [51, 52]. To demonstrate non-dispersive wave propagation, three different frequencies were sent out (6 MHz, 8 MHz and 10 MHz). For this purpose, five sinus waves were sent in the sample and the time taken for the receiving sensor to measure these waves was taken (Figure 34a). In non-dispersive media, the phase velocities are expected to be identical for all frequencies. Constant velocities of c = 6250 m/s were determined for all frequencies, which confirms the assumptions made. The associated frequency domain with the corresponding harmonic frequencies are shown in Figure 34b.

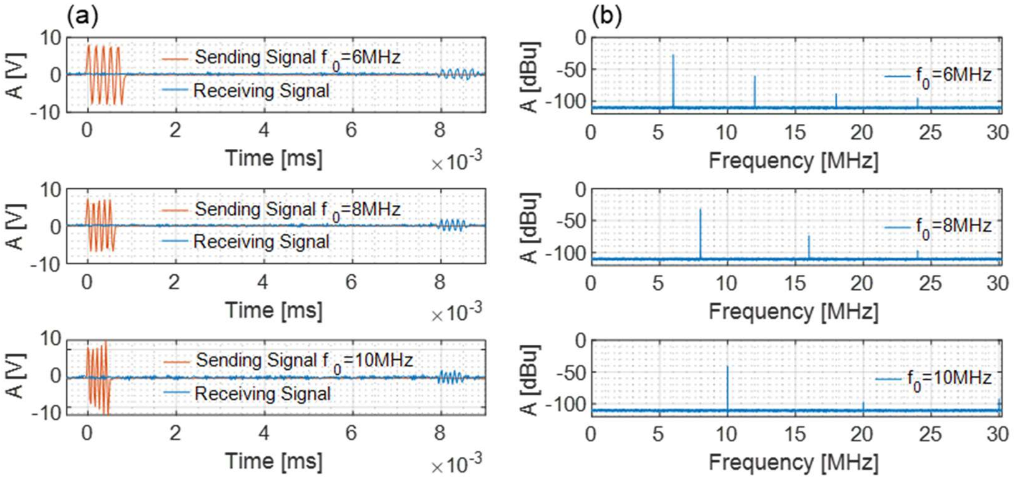

Figure 34. Proof of non-dispersive wave propagation: (a) time domain; (b) frequency domain.

4. Conclusion

The aim of this study was to develop a frequency-modulated ultrasound technique for the determination and characterization of plasticity in metallic materials. The wave equation with dual-frequency excitation was solved up to the third-order and was combined with the dislocation theory, which was further developed for higher dislocation orders. With two different excitation frequencies, the nonlinearity parameters for the frequencies $2f_{1,2}$, $3f_{1,2}$, $f_2 \pm f_1$, $2f_1 \pm f_2$ and $2f_2 \pm f_1$ were derived. In theory, defined nonlinearity parameters increase while other decrease with increasing plastic strain. This contrary behaviour was proven experimentally with flat tensile specimens made of stainless steel and Inconel 718 (plate and SLM manufactured). These were plastically deformed with different tensile loads and compared with reference samples. The behaviour of the determined nonlinearity parameters showed clear agreement with the theoretical observations. In addition, it was shown theoretically and experimentally that the behaviour of defined parameter values is reversed depending on the ultrasonic excitation direction. With the developed technique, the unique signature can reveal plastic zone in materials and also allows identification of the tensile load vector. This approach could be used to detect damage at an early stage in critical loaded structures, such as gas turbine components.

Acknowledgement

Thanks to the MAN Energy Solutions SE for their support.

Appendix A

In Section 2.2, the nonlinear relationship of the nonlinear Hooke's law ($\sigma = \alpha_d \varepsilon + \frac{1}{2}\beta_d \varepsilon^2 + \frac{1}{6}\gamma_d \varepsilon^3$) was shown, where the coefficient α_d with the values from Table 1 was compared with the Young's modulus *E* in the linear elastic deformation range (Figure A1). In the case of small strains, both values match. In the higher strain range, the α_d curve flattens out due to the influence of the plastic strain, as would also be expected in the typical plastic deformation behaviour of a metal.

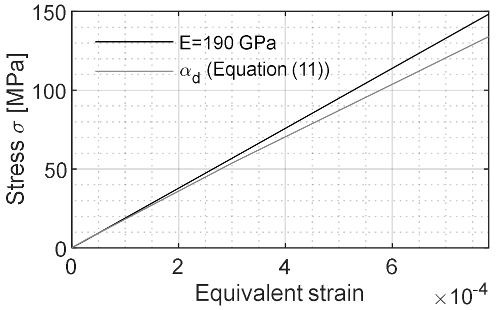

Figure A1. Comparison – Young's modulus with nonlinearity coefficient α_d.

Appendix B

The signature determined for the detection of plasticity in materials offers the possibility to differentiate the damage and allows statements about the possible load direction. In order to consider this in more detail, Figure B1a illustrates the behaviour of the normalized nonlinearity coefficients ($\alpha_d^{\parallel}$, $\beta_d^{\parallel}$ and $\gamma_d^{\parallel}$) with the given values as a function of the applied stresses. Coefficient $\gamma_d^{\parallel}$ increases with higher tensile load, whereas $\alpha_d^{\parallel}$ decreases in the positive range and $\beta_d^{\parallel}$ decreases in the negative range. Negative acoustic nonlinearities were also observed in [30], and a decaying nonlinearity behaviour with increasing plastic strain was discussed in [31, 33]. In the orthogonal ultrasonic excitation, Figure B1b reveals the coefficient values of $\alpha_d^{\perp}$, $\beta_d^{\perp}$ and $\gamma_d^{\perp}$. As with collinear excitation, the $\beta_d^{\perp}$ coefficient decreases into the negative range with an increasing load. Also $\gamma_d^{\perp}$ decreases while $\alpha_d^{\perp}$ increases in the negative range.

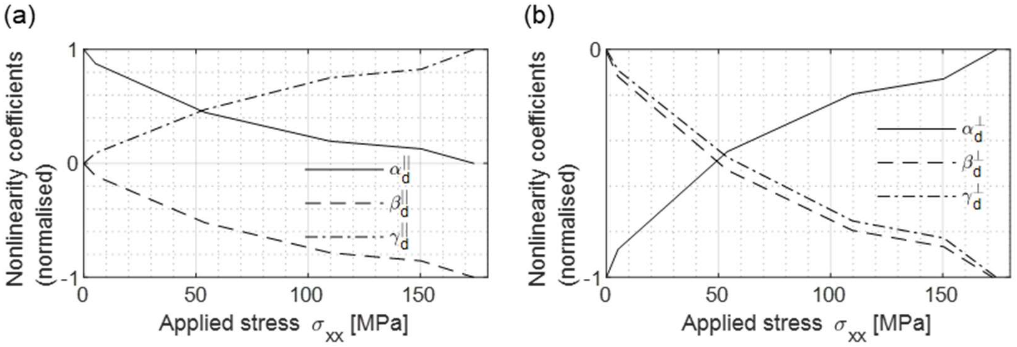

Figure B1. Behaviour nonlinearity coefficients: (a) collinear excitation; (b) orthogonal excitation.

References

1. Mevissen, F., & Meo, M. (2019). A Review of NDT/Structural Health Monitoring Techniques for Hot Gas Components in Gas Turbines. *Sensors, 19*(3), 711.
2. Langenecker, B. (1966). Effects of Ultrasound on Deformation Characteristics of Metals. *IEEE transactions on sonics and ultrasonics, 13*(1), 1–8.
3. Yang, Y., Ng, C.-T., & Kotousov, A. (2019). Second-order harmonic generation of Lamb wave in prestressed plates. *J. Sound Vib., 460*, 114903.
4. Eaves, A., Smith, A., Waterhouse, W., & Sansome, D. (1975). Review of the application of ultrasonic vibrations to deforming metals. *Ultrasonics, 13*(4), 162–170.
5. Kirchner, H., Kromp, W., Prinz, F., & Trimmel, P. (1985). Plastic deformation under simultaneous cyclic and unidirectional loading at low and ultrasonic frequencies. *Mater. Sci. Eng. C, 68*(2), 197–206.
6. Estrin, Y. (1998). Dislocation theory based constitutive modelling: foundations and applications. *J. Mater. Process. Technol., 80-81*, 33–39.
7. Jhang, K.-Y., & Kim, K.-C. (1999). Evaluation of material degradation using nonlinear acoustic effect. *Ultrasonics, 37*(1), 39–44.
8. Jhang, K. Y. (2000). Applications of nonlinear ultrasonics to the NDE of material degradation. *IEEE transactions on ultrasonics, ferroelectrics, and frequency control, 47*(3), 540–548.
9. Daud, Y., Lucas, M., & Huang, Z. (2006). Superimposed ultrasonic oscillations in compression tests of aluminium. *Ultrasonics, 186*(1-3), 179-190.
10. Ashida, Y., & Aoyama, H. (2007). Press forming using ultrasonic vibration. *J. Mater. Process. Technol., 187-188*, 118–122.
11. Oruganti, R. K., Sivaramanivas, R., Karthik, T. N., Kommareddy, V., Ramadurai, B., Ganesan, B., et al. (2007). Quantification of fatigue damage accumulation using non-linear ultrasound measurements. *Int. J. Fatigue, 29*(9-11), 2032–2039.
12. Pruell, C., Kim, J.-Y., Qu, J., & Jacobs, L. J. (2009). A nonlinear-guided wave technique for evaluating plasticity-driven material damage in a metal plate. *NDT Int., 42*(3), 199–203.
13. Deng, M., & Pei, J. (2007). Assessment of accumulated fatigue damage in solid plates using nonlinear Lamb wave approach. *Appl. Phys. Lett., 90*(12), 121902.
14. Pruell, C., Kim, J.-Y., Qu, J., & Jacobs, L. J. (2007). Evaluation of plasticity driven material damage using Lamb waves. *Appl. Phys. Lett., 91*(23).

15. Xiang, Y., Deng, M., Xuan, F.-Z., & Liu, C.-J. (2011). Cumulative second-harmonic analysis of ultrasonic Lamb waves for ageing behavior study of modified-HP austenite steel. *Ultrasonics, 51*(8), 974–981.

16. Rao, V. J., Kannan, E., Prakash, R. V., & Balasubramaniam, K. (2009). Observation of two stage dislocation dynamics from nonlinear ultrasonic response during the plastic deformation of AA7175-T7351 aluminum alloy. *Mater. Sci. Eng., 512*(1-2), 92–99.

17. Kim, C.-S., & Jhang, K.-Y. (2012). Fatigue-Induced Micro-damage Characterization of Austenitic Stainless Steel 316 Using Innovative Nonlinear Acoustics. *Chinese Physics Letters, 29*(6), 60702.

18. Yao, Z., Kim, G.-Y., Faidley, L., Zou, Q., Mei, D., & Chen, Z. (2012). Effects of superimposed high-frequency vibration on deformation of aluminum in micro/meso-scale upsetting. *J. Mater. Process. Technol., 212*(3), 640–646.

19. Yao, Z., Kim, G.-Y., Wang, Z., Faidley, L., Zou, Q., Mei, D., et al. (2012). Acoustic softening and residual hardening in aluminum: Modeling and experiments. *Int. J. Plast., 39*, 75–87.

20. Walker, S. V., Kim, J.-Y., Qu, J., & Jacobs, L. J. (2012). Fatigue damage evaluation in A36 steel using nonlinear Rayleigh surface waves. *NDT & E International, 48*, 10–15.

21. Jaya Rao, V. V. S., Kannan, E., Prakash, R. V., & Balasubramaniam, K. (2008). Fatigue damage characterization using surface acoustic wave nonlinearity in aluminum alloy AA7175-T7351. *J. Appl. Phys., 104*(12), 123508.

22. Dutta, R. K., Petrov, R. H., Delhez, R., Hermans, M., Richardson, I. M., & Böttger, A. J. (2013). The effect of tensile deformation by in situ ultrasonic treatment on the microstructure of low-carbon steel. *Acta Materialia, 61*(5), 1592–1602.

23. Hong, M., Su, Z., Wang, Q., Cheng, L., & Qing, X. (2014). Modeling nonlinearities of ultrasonic waves for fatigue damage characterization: theory, simulation, and experimental validation. *Ultrasonics, 54*(3), 770–778.

24. Xiang, Y., Zhu, W., Liu, C.-J., Xuan, F.-Z., Wang, Y.-N., & Kuang, W.-C. (2015). Creep degradation characterization of titanium alloy using nonlinear ultrasonic technique. *NDT & E International, 72*, 41–49.

25. Hikata, A., Chick, B. B., & Elbaum, C. (1965). Dislocation Contribution to the Second Harmonic Generation of Ultrasonic Waves. *J. Appl. Phys., 36*(1), 229–236.

26. Hikata, A., & Elbaum, C. (1966). Generation of Ultrasonic Second and Third Harmonics Due to Dislocations. I. *Physical Review, 144*(2), 469–477.

27. Cantrell, J. H. (2009). Nonlinear dislocation dynamics at ultrasonic frequencies. *J. Appl. Phys., 105*(4), 43520.

28. Apple, T. M., Cantrell, J. H., Amaro, C. M., Mayer, C. R., Yost, W. T., Agnew, S. R., et al. (2013). Acoustic harmonic generation from fatigue-generated dislocation substructures in copper single crystals. *Philosophical Magazine, 93*(21), 2802–2825.

29. Cash, W. D., & Cai, W. (2011). Dislocation contribution to acoustic nonlinearity: The effect of orientation-dependent line energy. *J. Appl. Phys., 109*(1), 14915.

30. Cash, W. D., & Cai, W. (2012). Contribution of dislocation dipole structures to the acoustic nonlinearity. *J. Appl. Phys., 111*(7), 74906.

31. Xiang, Y., Deng, M., Liu, C.-J., & Xuan, F.-Z. (2015). Contribution of mixed dislocations to the acoustic nonlinearity in plastically deformed materials. *J. Appl. Phys., 117*(21), 214903.

32. Zhang, J., & Xuan, F.-Z. (2014). A general model for dislocation contribution to acoustic nonlinearity. *EPL (Europhysics Letters), 105*(5), 54005.

33. Zhang, J., Xuan, F.-Z., & Xiang, Y. (2013). Dislocation characterization in cold rolled stainless steel using nonlinear ultrasonic techniques: A comprehensive model. *EPL (Europhysics Letters), 103*(6), 68003.

34. Zhu, W., Deng, M., Xiang, Y., Xuan, F.-Z., Liu, C., & Wang, Y.-N. (2016). Modeling of ultrasonic nonlinearities for dislocation evolution in plastically deformed materials: Simulation and experimental validation. *Ultrasonics, 68*, 134–141.

35. Gao, X., & Qu, J. (2018). Acoustic nonlinearity parameter induced by extended dislocations. *J. Appl. Phys., 124*(12), 125102.

36. Mevissen, F., & Meo, M. (2019). Detection of Cracks in Turbine Blades with Nonlinear Ultrasonic Frequency Modulation. In *IWSHM 2019, Stanford, USA, 10-12 September 2019*. (pp. 824–834): DEStech Publications Inc.

37. Mevissen, F., & Meo, M. (2020). A Nonlinear Ultrasonic Modulation Method for Crack Detection in Turbine Blades. *Aerospace, 7*(6), 72.

38. Frank, F. C., & Read, W. T. (1950). Multiplication Processes for Slow Moving Dislocations. *Physical Review, 79*(4), 722–723.

39. Luo, L., & Ghosh, A. K. (2003). Elastic and Inelastic Recovery After Plastic Deformation of DQSK Steel Sheet. *J. Eng. Mater. Technol., 125*(3), 237–246.

40. Mishakin, V. V., Klyushnikov, V. A., & Gonchar, A. V. (2015). Relation between the deformation energy and the Poisson ratio during cyclic loading of austenitic steel. *Technical Physics, 60*(5), 665–668.

41. Yang, M. X., Yuan, F. P., Xie, Q. G., Wang, Y. D., Ma, E., & Wu, X. L. (2016). Strain hardening in Fe–16Mn–10Al–0.86C–5Ni high specific strength steel. *Acta Mater., 109*, 213–222.

42. Cantrell, J. H. (2014). Elastic constants of solids and fluids with initial pressure via a unified approach based on equations-of-state. *Ultrasonics, 54*(5), 1323–1331.

43. Cantrell, J. H., & Yost, W. T. (2013). Acoustic nonlinearity and cumulative plastic shear strain in cyclically loaded metals. *J. Appl. Phys., 113*(15), 153506.

44. Symon, K. R. (1980). *Mechanics*. (3rd edn, Addison-Wesley world student series edition). Reading, Mass: Addison-Wesley.

45. Crecraft, D. (1967). The measurement of applied and residual stresses in metals using ultrasonic waves. *J. Sound Vib., 5*(1), 173–192.

46. Abbasi, Z., & Ozevin, D. (2016). The influence of ultrasonic frequency on shear stress measurement using acoustoelasticity, *1706*(1).

47. Mevissen, F., & Meo, M. (2021). Nonlinear Ultrasound Crack Detection with Multi-Frequency Excitation—A Comparison. *Sensors, 21*(16), 5368.

48. Viswanath, A., Rao, B. P. C., Mahadevan, S., Parameswaran, P., Jayakumar, T., & Raj, B. (2011). Nondestructive assessment of tensile properties of cold worked AISI type 304 stainless steel using nonlinear ultrasonic technique. *J. Mater. Process. Technol., 211*(3), 538–544.

49. Shintani, T., & Murata, Y. (2011). Evaluation of the dislocation density and dislocation character in cold rolled Type 304 steel determined by profile analysis of X-ray diffraction. *Acta Materialia, 59*(11), 4314–4322.

50. Cleveland, R., & Ghosh, A. (2002). Inelastic effects on springback in metals. *Int. J. Plast, 18*(5-6), 769–785.

51. Cheeke, J. D. N. (2002). *Fundamentals and applications of ultrasonic waves*. (CRC series in pure and applied physics). Boca Raton, FL, USA: CRC Press.

52. Rose, J. L., & Nagy, P. B. (2000). Ultrasonic Waves in Solid Media. *J. Acoust. Soc. Am., 107*(4), 1807–1808.